POLITECHNICO DI TORINO

Master's Degree in Mechanical Engineering

Master's Degree Thesis

Secondary atomization and solidification of metal melt in gas atomization

Supervisors

Prof. Daniela Anna MISUL

Dr. G. FINOTELLO

Ir. D.P.L. THUY

Candidate

Seyedhamed ABDOLLAHI

Nov. 2023

EINDHOVEN UNIVERSITY OF TECHNOLOGY

Department of Mechanical Engineering
Group of Power & Flow - Group Deen

Secondary atomization and solidification of metal melt in gas atomization

Master Thesis

Seyedhamed Abdollahi

Supervisors:
Dr. G. FINOTELLO
Prof. Daniela MISUL
Ir. D.P.L. THUY

Eindhoven, November 2023

Abstract

A gas atomizer is a device used to disperse a stream of molten metal into fine powder particles. Understanding and optimizing the atomization of metal powders are essential steps to enhance the quality and performance of AM-produced components. The breakup of the molten metal can be divided in two stages, primary and secondary atomization. In the primary stage, the liquid jet disintegrates into ligaments and larger droplets. The secondary breakup involves the fragmentation of these larger droplets into finer particles. In this secondary stage, the droplet breakup to fine particles and then cools down to solid state before reaching the bottom of the atomization chamber. The core objective of the thesis is centered on the modelling of the process of secondary breakup followed by solidification within a gas atomizer, using the lagrangian solver available in the open-source CFD software "OpenFOAM." The project consists of two key phases. In the initial phase, the focus lies on modelling and validating the secondary breakup of a liquid metal droplet. This involves integrating the Taylor Analogy Breakup (TAB) and implementing the Kelvin-Helmholtz (KH) mechanism, following the model described by Liu et. al [1]. The validation model is based on Benz UCF-I test fuel (SAE J967d). Further modeling on solidification is conducted with iron, and its properties have been added to the software's thermodynamic library. As there is no available class/solver to handle the solidification of the broken-up droplets, the second phase involves developing a novel class within Lagrangian library for such modelling to transition the phase of liquid droplets to solid ones. This new class draws from the investigated phenomena and the derived equations concerning solidification and recalescence from the literature.

Acknowledgements

This thesis contributes to the PhD project Supervisored by D. Thuy, who is engaged in the comprehensive study and modeling of gas atomization processes. I am sincerely grateful to dr. Guilia Finotello and Dennis Thuy for their invaluable guidance and mentorship throughout this research. Also extend special thanks to Professor Daniela Anna Misul from Politecnico di Torino for her support during my research at TU/e. Additionally, I would like to acknowledge the DENERG at Polito and the Power and Flow Group at TU/e for providing me with a conducive environment to pursue my thesis.

Lastly, I would like to express my gratitude to all PhD students participanting to our weekly OpenFOAM meetings. Their advice and collaborative thinking played an instrumental role in making this possible.

"Sicerely,"
Hamed Abdollahi

Table of Contents

List of Tables

List of Figures

Chapter 1

Introduction

Additive manufacturing also known as 3D printing has become popular over the past decades. The process of additive manufacturing uses layer by layer deposition of material and produces products directly from 3D model. The considered technology has capability for manufacturing products with complexity and with high precision in short time. Therefore, additive manufacturing is widely used in numerous research fields ranging from biomedical, mechanical engineering and chemistry to material science. In case of metal 3D printing, metal powders are used as main material to produce the product [2, 3].

1.1 Metal powders for AM

1.1.1 Introduction

The powder bed fusion (PBF) is a type of additive manufacturing technology (as outlined by the ISO/ASTM 52900:2015 standard) where thermal energy is used to strategically fuse regions of a powder bed, as seen in the Figure 1.1 [2]. PBF is widely used for manufacturing complex geometries because of high dimensional accuracy and capability for topology optimization [4].

One of the different additive manufacturing techniques that fall under this category is selective laser melting (SLM), which selectively heat powders uniformly spread over the table as needed by using laser as the source of heat. As each layer is deposited, the powder bed is indexed downward by the thickness of the constructed layer, and a new layer of powder is deposited over the entire length. Powder spreading is typically accomplished using a roller or blade, ensuring a uniform layer over the previous as-built layer. The mechanical characteristics of the final product are predominantly influenced by both the powder's characteristics and the printing parameters [4, 5]. In SLM, a distinct "remelted zone" facilitates

bonding between newly melted and solidified material, as shown in the Figure 1.1.

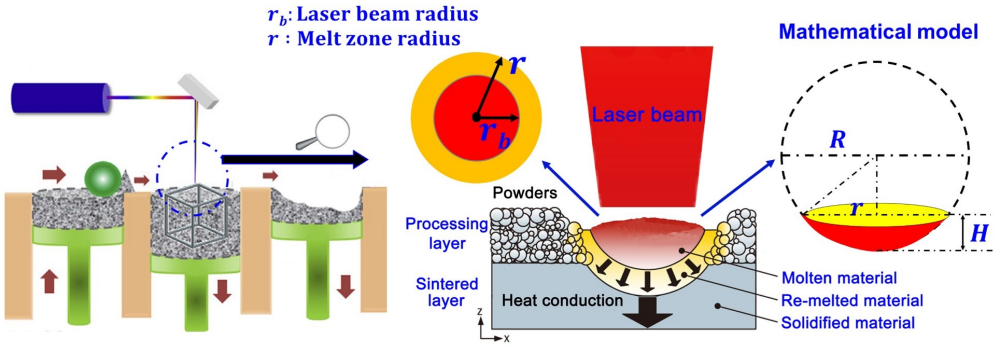

Figure 1.1: 3D Printing: Layer-by-layer application of liquid binder onto thin powder layers to create 3D objects. Picture taken from Tan et al.[5]

The first challenge in using powder mixtures is the quality of each powder. Optimal powders for powder bed techniques are spherical to enable a good flowability with particle size distribution (PSD) roughly in the range of 20-45 µm, although the quality of these properties is more relevant in the powder bed techniques [4].

In the effort to optimize the atomization process and achieve effective material reuse, a challenge emerges from the waste recycling point. A significant amount of powder isn't used in each cycle because of it is poor flowability, making it unsuitable for reuse. Also, taking away support structures meant to prevent bending due to thermal stresses can increase waste, and thus damaging the final part due to removal of support structure [6, 7].

There are several methods for metal powder production and one of the popular methods is atomization method. Among the four main processes known as "gas atomization", "water atomization", "centrifugal atomization" and "plasma atomization", the first one was taken into consideration for this thesis. 3D printing applications have driven innovations in particle technology, especially through tackling particle-related issues arising from solidification time, recalescence, and satellite formation. In our study we only produce feedstock for 3D printing [2, 8].

The solidification of these fine particles through atomization after breakup has received limited attention in the existing literature. Hence, the key objective of this study is to develop a model for this process. To achieve this goal, we must initially calibrate our computational models and validate them for the breakup mechanism.

1.1.2 Types of atomization process

The production of fine metal powders is achieved through various atomization techniques, each with distinct characteristics. Four prominent methods are discussed

in literature: water atomization, centrifugal atomization, gas atomization [9], and plasma atomization [10, 11]. The choice among these techniques depends on factors such as energy input for shearing the melt into droplets [11], scalability, ease of operation, and powder properties.

Water atomization as shown in Figure 1.2 involves introducing metal melt from above, where water jets impact the melt stream, atomizing and solidifying the metal [10]. Scalability, in this context, refers to the ability to adapt this atomization process to different production scales or sizes. This specifically makes the scalability limitation only in one direction, since the solidification rate dictates the dimension of dispersion. Water atomization is known for its higher cooling rate, leading to shorter particle trajectories to solidify, yet requires drying for the resultant powder [11]. This process, though efficient, can yield irregular particle shapes due to rapid solidification [12].

Gas atomization (Figure 1.3) has gained significant attention due to its high industrial production rates [8]. It yields a wider Particle Size Distribution (PSD) compared to advanced atomization types such as centrifugal and plasma atomization. Gas atomization produces spherical particles, making it suitable for additive manufacturing (AM) applications, but challenges like satellite formation need to be addressed in the atomizer's design.

In centrifugal atomization (Figure 1.5), a rapidly rotating disk disperses molten metal, leading to atomization through shear forces [12]. This technique is limited by equipment size due to the need to prevent droplet splattering caused by droplets hitting the wall chamber (scalability limitation size). Centrifugal atomization yields a narrow Particle Size Distribution (PSD), and its overall particle size is influenced by the rotational speed of the disk [11].

Plasma atomization (Figure 1.4) involves melting and atomizing solid metal wire or powder using gas jets and plasma torches [11]. This technique offers the ability to produce smaller diameter particles than gas atomization, but it requires the metal to be fed in a processed form, such as wire. Plasma atomization presents a unique combination of melting and atomization steps.

Particle Size Distribution (PSD) plays a crucial role in determining powder properties. Centrifugal atomization offers a narrow PSD, while gas atomization tends to have a wider distribution [12]. Water atomization yields irregular particle shapes due to rapid solidification, while gas atomization produces spherical particles, aligning well with AM requirements [12]. In the Figure 1.6 a comparison over particles sphericity for each method is presented.

In gas and water atomization represented in the Figure 1.6, it is evident that smaller droplets, referred to as satellites, are fused to larger droplets. Satellite particles are formed due to the difference in acceleration of small droplets compared to large ones in the gas flow, leading to collisions [16]. It can be seen that at temperatures above the liquidus temperature, small particles can still be enveloped

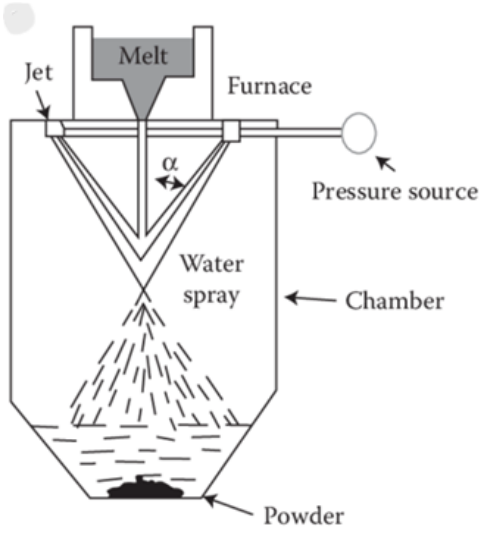

Figure 1.2: Water Atomization [13]

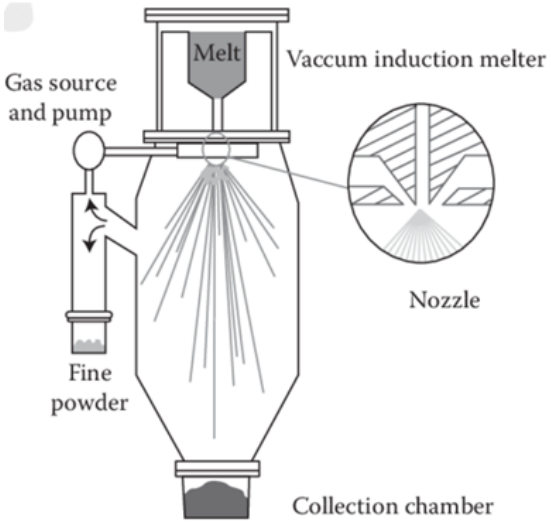

Figure 1.3: Gas Atomization [13]

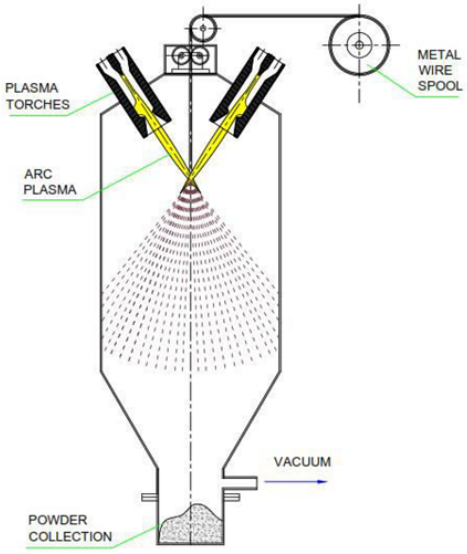

Figure 1.4: Plasma Atomization [14]

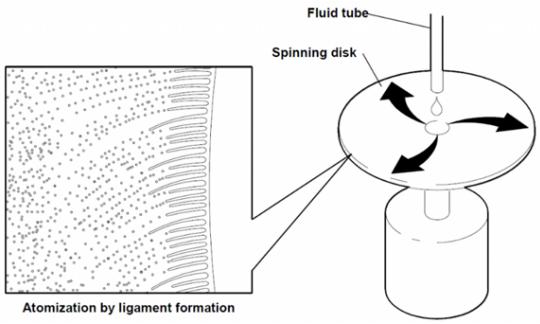

Figure 1.5: Centrifugal Atomization [15]

in the liquid sphere. However, as the droplet temperature decreases and solidification starts to take place, the satellite particle manifests itself on the surface of the larger droplet, thus decreasing the sphericity of the resulting particle. This type of behavior can affect both particle morphology and particle size distribution of the powder. When focussing on AM, the presence of satellite particles reduces the flowability of the powder, due to irregularity of the powder [17].

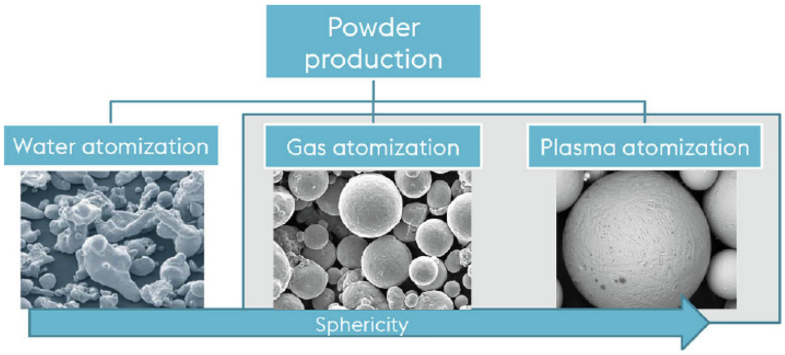

Figure 1.6: Shapes of different metal powders [18]

In summary, the various atomization processes offer distinct advantages and disadvantages, with considerations including cost resulting from using non ingot form of feedstock in plasma atomization and larger chamber use for centrifugal atomization, ease of operation, scalability, particle size, morphology, and PSD. By understanding these factors as represented in the table 1.1, manufacturers can make informed choices in selecting the most suitable atomization technique for their specific applications [10, 9, 11, 12, 8, 2].

Atomization / **Characteristic**	**Water**	**Gas**	**Centrifugal**	**Plasma Aided**
Ingot Form Input	✓	✓	✓	×
Unified Melting + Atomization	×	×	×	✓
1D Scalability	✓	✓	×	✓
Spherical Particles (Morphology)	×	✓	✓	✓
PSD (Size range in µm)	✓ (0–500)	✓ (0–500)	× (0–600)	✓ (0–200)
Drying Needed	✓	×	×	×
Satellite Formation	✓	✓	×	×

Table 1.1: Atomization Techniques Comparison, data extracted from [2]

Gas atomization emerges as a preferred technique for AM technology due to its ability to fulfill the major industry needs for sufficiently fine powders plus it has low fixed cost and less complexity compared to plasma and centrifugal types. The flexibility to use reactive alloys further endorses its viability [8, 9].

1.2 Gas atomization

In Gas atomization, a metal melt stream is introduced into a spraying chamber through an orifice. Subsequently, the melt is disintegrated by the impact of high-velocity jets of inert gas [19]. The interaction between the atomizing gas and the melt leads to rapid cooling rates ranging from approximately 10^3 to 10^4 K/s and deep undercooling of the particles [20]. As a result, particles exhibit reduced segregation and a refined microstructure, enhancing properties such as toughness, hardness, and strength [19, 21].

As shown in the Figure 1.7, primary atomization involves the disruption of the gas-melt interface due to turbulence and aerodynamic forces, resulting in the separation of ligaments from the jet's surface. The breakup of these ligaments into smaller droplets further downstream is the secondary atomization, or secondary breakup [22].The gas atomization process clearly involves several length scales, as evident from these subsequent breakup events. Moreover, the supersonic injection of gas leads to highly coupled turbulent flows, giving rise to a multi-scale issue. [23].

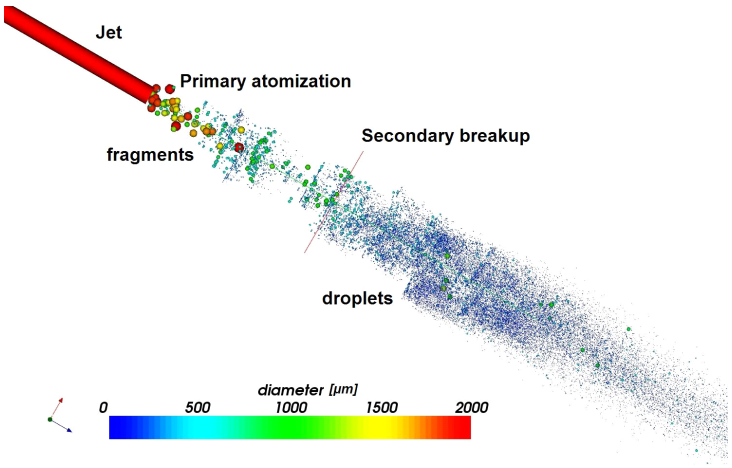

Figure 1.7: Schematic of atomization process 3D [24].

1.2.1 Configuration

The design and configuration of atomizers play a crucial role in determining the characteristics of the produced powders. In the gas atomization, two prominent configurations stand out: the free-fall and close-coupled atomization setups.

1. Free-Fall: In this configuration as shown in the Figure 1.8 (a), the metal melt jet descends from the orifice under the influence of gravity, traveling a

significant distance (typically 10-30 cm) before encountering the impinging gas jets. The advantage of this setup lies in its minimal risk of issues like backflow and melt freeze-off (due to lower likelihood of encountering counterflows or disturbances) [25].

2. Close-Coupled: Contrasting with the free-fall approach, the close-coupled configuration as shown in the Figure 1.8 (b) involves the direct impact of gas jets on the melt stream as it exits the melt tube. This design often leads to the production of finer powders compared to the free-fall counterpart (due to direct impingement with higher momentum of the gas jet right after it exits the nozzle) [21].

The close-coupled atomizer is favored for additive manufacturing (AM) due to its ability to produce finer powders, aligning well with the demands of AM processes [21].

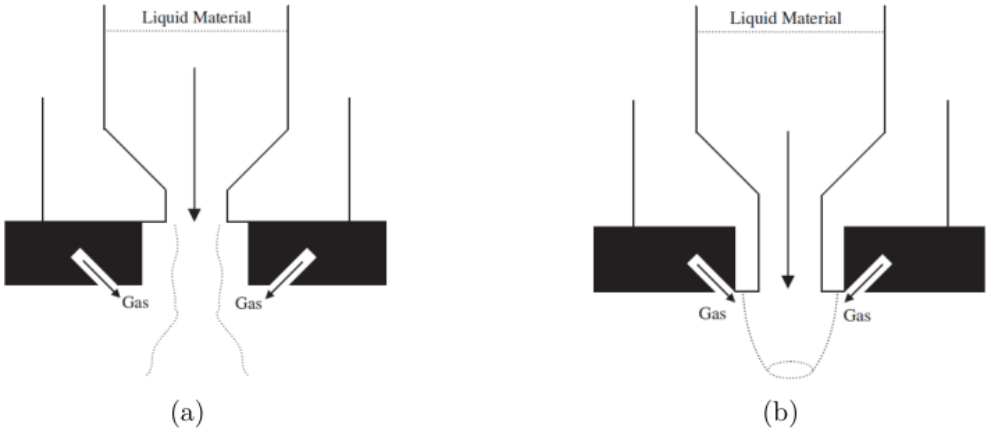

Figure 1.8: Schematics of the free-fall (a), and the close-coupled (b) atomizer [25]

1.2.2 Gas Dynamics

Extensive research has focused on gas-only flows in atomizers to grasp the complex flow dynamics of supersonic gases and their impact on droplet trajectories and atomization.

Figure 1.9 offers an overview of velocity contours by Thompson et al. concerning the velocity field of the gas near a close-coupled gas nozzle [26, 27, 28]. According to the Prandtl-Meyer theory, gas flow entering the atomization chamber undergoes expansion due to lower pressure in the atomization chamber. This expansion leads to a sequence of waves and oblique shocks, creating a complex fluid dynamics environment within the chamber [26].

The presence of shock waves introduces certain complexities. In cases where shock waves are prominent, a significant amount of the kinetic energy of the gas is dissipated within the shock wave itself. This energy loss can negatively impact the atomization process, leading to the production of larger droplets and potentially less desirable particle characteristics.[29]

To mitigate these effects and optimize the atomization process for the production of finer particles, the control and manipulation of shock waves become crucial. However, upon introducing the melt into the model as shown in the Figure 1.10, following outcomes emerge:

- Shock Wave Absence: Shock waves are notably absent during the introduction of the melt.[29]
- Moderated Gas Expansion: The expansion of the gas experiences a reduction due to the injection of the melt. The absence of a well-defined sharp edge in this scenario curtails the gas's tendency to expand, which otherwise triggers the formation of a series of shock waves.[26]
- Suppressed Axial Velocity: The axial velocity within the recirculation zone is significantly subdued.[26]
- Reduced Downstream Gas Velocities: Downstream gas velocities register a considerable decrease. This reduction in velocity is also attributed to the transfer of kinetic energy from the gas to the accelerating melt, resulting in a dissipation of the gas's kinetic energy.[29]

These outcomes underscore the intricate interplay between the introduced melt and the gas dynamics, shaping the flow characteristics and shock wave behavior within the system.

1.2.3 Turbulence modeling

In the gas atomization, turbulence plays a crucial role in shaping the process dynamics. Large-scale eddies, responsible for transferring kinetic energy from the gas phase to the liquid, induce stretching and fragmentation of liquid droplets [31]. These inherently three-dimensional structures challenge the adequacy of traditional two-dimensional simulations [25, 32]. Therefore, capturing gas-phase turbulence accurately is vital. Yet, research on turbulence modeling in atomization systems is relatively limited. Zhao et al. offer insights into the suitability of different turbulence models, including Direct Numerical Simulation (DNS), Large Eddy Simulation (LES), and Reynolds-Averaged Navier-Stokes (RANS) formulations [33].

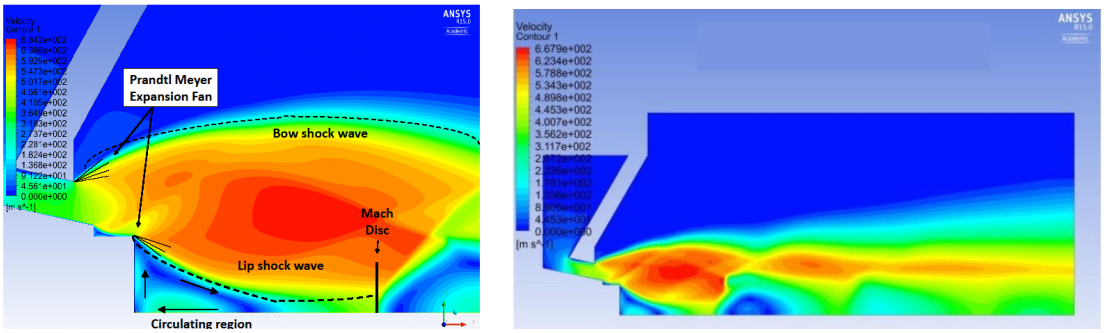

(a) (b)

Figure 1.9: Velocity contours depicting the gas-only flow fields in close-coupled configurations. The gas flow is axisymmetrical, as demonstrated in a region near to the gas nozzle exit. [27]

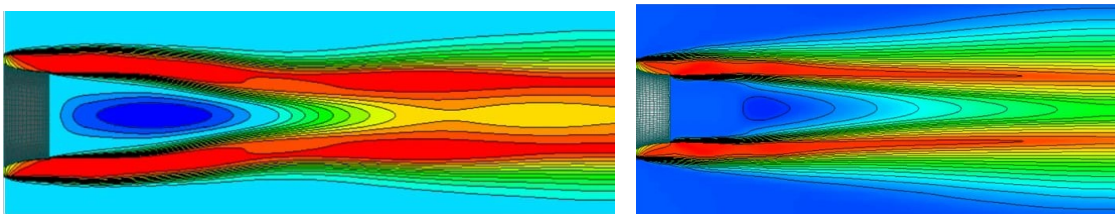

(a) (b)

Figure 1.10: Velocity contours describing the gas flow characteristics without melt flow (a) with a melt inlet flow rate of 0.20 kg/s (b) [30]

Direct Numerical Simulation (DNS) stands out as a powerful technique where all turbulent scales are resolved, eliminating the need for additional turbulence models. It offers exceptional accuracy in capturing turbulence phenomena. However, it comes at the cost of extensive computational resources and is less commonly employed in supersonic gas atomization studies.[28-31]

Large Eddy Simulation (LES) represents a robust approach for numerically studying turbulent flows. This method assumes that large eddies play a significant role in transporting momentum, mass, and energy, while smaller eddies exhibit more isotropic behavior. In LES, we explicitly compute large eddies and model the effects of small eddies. This approach provides higher accuracy compared to Reynolds-Averaged Navier-Stokes (RANS) modeling.[30, 33]

In the context of gas atomization, the predominant approach to turbulence modeling is Reynolds-Averaged Navier-Stokes (RANS). RANS models the entire spectrum of turbulent scales by representing them as the transport of average flow quantities. While it simplifies the computational demands, it may not capture fine-scale turbulence as effectively as DNS or LES methods.

1.2.4 Melt Dynamics

To analyze breakup phenomena accurately, we begin by introducing key dimensionless parameters. One such parameter, the Weber number (defined in equation 1.1), characterizes the balance between gas-phase inertia and surface tension forces. It is widely used for classifying breakup phenomena in spray technology.

$$We = \frac{\rho u_{rel}^2 d_p}{\sigma} = \frac{\text{Gas phase inertia}}{\text{Surface tention forces}} \tag{1.1}$$

where ρ is the gas (liquid in case of We_l) density, u_{rel} is the relative velocity between gas and liquid phases, d_p is the droplet diameter, and σ is the surface tension. The Reynolds number, as shown in equation 1.2, is the ratio between inertia and viscous forces:

$$Re = \frac{\rho u_{rel} d_p}{\mu_g} = \frac{\text{Inertia Forces}}{\text{Viscous forces}} \tag{1.2}$$

Where μ_g gas dynamic viscosity. The Ohnesorge number combines the effects of inertia, viscosity, and surface tension in the spray liquid:

$$Oh = \frac{\sqrt{We_l}}{Re_l} = \frac{\mu_l}{\sqrt{\rho \sigma d_p}} = \frac{\text{Kinetic energy}}{\text{Energy dissipation by viscous flow}} \tag{1.3}$$

Please note that the relative velocity between the gas and droplet should be considered when calculating these values, and it should be ensured that clarity is maintained regarding whether the gas or liquid droplet is being referred to when these values are used in equations (e.g whether it is liquid or gas density).

1.2.5 Primary atomization

Primary breakup phenomena can be comprehensively analyzed through various models. One of these models is the linear stability theory , which is represented mathematically by complex functions [34]. However, it is important to note that phenomenological models like linear stability theory may have limitations, particularly when dealing with high Weber numbers.

An alternative approach to investigate primary breakup is through Volume of Fluid (VOF) numerical modeling. This method provides an accurate description of the interface between gas and melt. In VOF modeling, the gas-melt interface is tracked using an advection equation for the color function, denoted as 'f.' This function, serves to represent the gas volume fraction, with the value of 'f' being 0 within the melt, 1 within the gas phase, and having intermediate values between 0 and 1 at the interface. This equation is simultaneously solved alongside the continuity and Navier-Stokes equations [35]. It is worth mentioning that while

VOF modeling offers high accuracy, its performance decreases when dealing with dimensions that fall below the computational resolution [36].

1.2.6 Secondary atomization

Enhancing the understanding of secondary breakup phenomena is essential in the context of atomization processes. The velocity difference between the droplet and the ambient gas leads to uneven pressure distribution across the droplet's surface, accelerating the droplet, which is what happens in this stage. Consequently, dynamic forces become larger than surface tensions, leading to the fragmentation of the parent droplet [37]. As the relative velocity between the gas and melt decreases compared to the primary breakup stage, it leads to a lower Weber number. To comprehensively describe this phenomenon, we employ phenomenological models, specifically the Taylor-Analogy breakup (TAB), Kelvin-Helmholtz (KH), and Rayleigh-Taylor (RT) models. [38].

The primary atomization process sets the initial conditions, resulting in the formation of a spray. In our study, we make the assumption that the droplets are small and spherical after primary breakup, justifying the use of the Lagrangian method.

It is worth noting that the droplet breakup regimes are directly proportional to the Weber number. In conventional liquids, experimental data indicate minimal distinctions in the breakup modes and behavior of liquid metal droplets. These regimes include bag breakup at low Weber numbers, multimode breakup at slightly higher values, sheet stripping at further elevated Weber numbers, and catastrophic breakup at very high Weber numbers, driven by unstable surface waves. By looking at the Figure 1.11, these breakup modes can described as follows:

1. Bag breakup: Characterized by the formation of a thin, bag-like structure, further leading to a ring formation and eventually break up to finer particles.

2. Multimode breakup: Involves a bag formation paired with the presence of a stretched ligament in the center which further follows the fragmentation process of bag breakup.

3. Sheet stripping: Occurs when peripheral ligaments disintegrates to finer particles in which allowing the parent droplet to remain larger due to decreased aerodynamic forces.

4. Catastrophic breakup: Initiates from an unstable surface wave and culminates in complete fragmentation.

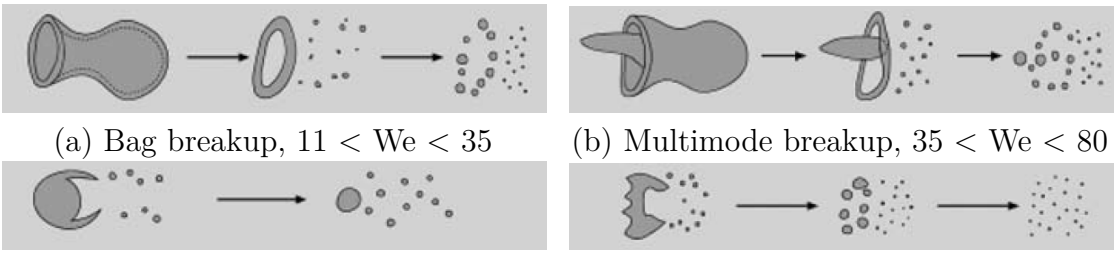

(a) Bag breakup, $11 < We < 35$ (b) Multimode breakup, $35 < We < 80$

(c) Sheet stripping, $80 < We < 350$ (d) Catastrophic breakup, $We > 350$

Figure 1.11: Droplet breakup modes for different ranges of Weber number [37]

Comparison between TAB and KH

The TAB model, developed by O'Rourke and Amsden, characterizes the interplay between aerodynamic and surface tension forces as a forced spring-mass system [39]. It equates surface tension to the spring force and aerodynamic forces to external forces, with droplet viscosity acting as damping. Breakup is determined based on energy conservation if the distortion exceeds a critical value [27]. For higher Weber numbers ($We > 80$), the KH model or combined KH-RT model is favored.

The KH model associates breakup time and droplet sizes with the fastest-growing instability wavelength, usually responsible for the breakup. It accounts for Kelvin-Helmholtz instabilities causing droplet shedding and considers Rayleigh-Taylor instabilities for sudden droplet acceleration. Breakup occurs if instabilities grow longer than a calculated breakup time and their wavelength is smaller than the parent droplet diameter [27, 26].

Simulation results using these models often yield a log-normal particle size distribution (PSD) [46]. Nevertheless, Firmansyah et al. found a bimodal PSD, attributing it to differences between coarser parent droplets and smaller child droplets [26].

Some variations exist when comparing the KH-RT model to a combination of the TAB and KH models, leading to differences in predicted breakup times and PSDs at various positions in the atomizer [22]. Both models generally result in a cone-shaped spray cloud, but the KH-TAB model shows a narrow track of larger droplets along the longitudinal axis and a size discontinuity at $We = 80$ [27].

Across different breakup models, certain trends emerge regarding process parameter effects on PSD and average particle size. Higher atomization gas pressure often leads to increased atomization rates and finer metal powders [40]. Conversely, an increased melt flow rate typically results in coarser powder production [27, 26].

Coupling

In the coupling the VOF (Volume of Fluid) method for primary breakup with Lagrangian methods for secondary breakup, two primary approaches come to the fore: the Direct Coupling Approach (DCA) and the Statistical Coupling Approach (SCA) [41].

As shown in the Figure 1.12 (b), the DCA is characterized by its precision in representing individual liquid structures during the atomization process. It accomplishes this by applying specific criteria for the evaluation of each droplet. When a droplet meets these criteria, it is seamlessly transferred from the Eulerian to the Lagrangian domain, especially where both representations overlap, facilitating the selection of the most accurate description for liquid structures. However, this approach can lead to higher computational costs [41].

In contrast, SCA prioritizes computational efficiency by shortening VOF simulations to reach statistical convergence and introducing Lagrangian particles based on this data. SCA often employs a stochastic parcel method to represent groups of droplets within the Lagrangian Particle Tracking (LPT) framework. Figure 1.12 (b) provides a visual representation of this method. This method offers a notable computational advantage due to its shortened VOF simulation time. Nevertheless, it is important to acknowledge that SCA is less suited for capturing transient spray behavior. Additionally, successful SCA application relies on precisely positioning the coupling plane within the system to align with a spray dilution phase, justifying the VOF to LPT transition. The challenge lies in the fact that not all spray structures reach this dilution phase simultaneously [42].

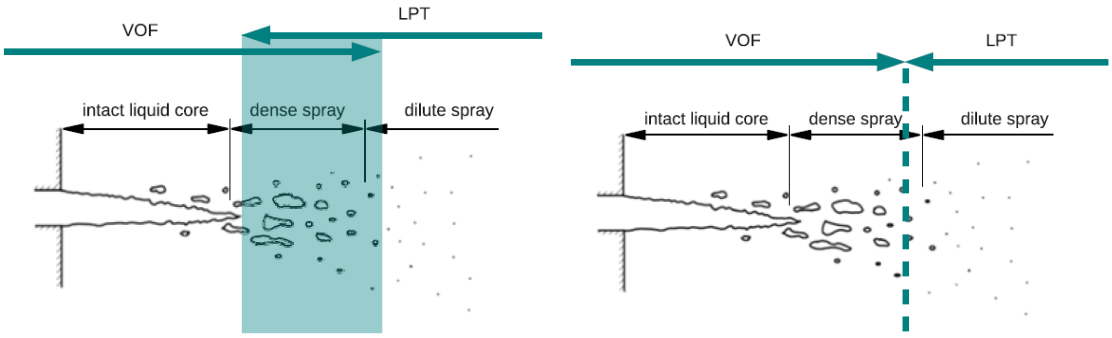

(a) DCA Coupling (b) SCA Coupling

Figure 1.12: Illustration of the methods for coupling primary and secondary breakup [41]

The choice between these two coupling methods hinges on the specific characteristics of the gas atomization process under investigation. SCA excels in terms of computational efficiency but may not capture transient behaviors effectively.

Conversely, DCA provides precise representation for individual liquid structures but may involve higher computational costs. Researchers like Heinrich et al. have successfully employed both methods in various studies, achieving favorable agreement with experimental data regarding droplet characteristics such as the Sauter mean diameter and particle size distribution incorporating DCA coupling [22]. However, for the context of close-coupled gas atomization, where interface capturing methods like VOF are integrated with Lagrangian methods, the preferred coupling method ultimately depends on the statistical nature of the gas atomization process and the feasibility of defining an appropriate location for the coupling plane [41, 42].

1.2.7 Cooling and Solidification

The presence of a high temperature gradient (∇T) significantly influences how particles behave during the cooling process and what final powder properties would be, ultimately making solidification a crucial factor in determining the final properties of powdered materials.

By not integrating the solidification model with the secondary breakup process in the atomizer, we overlook the most substantial impact of solidification on powder properties. The competition between droplet breakup and cooling and solidification rates plays a significant role in determining the size and shape of the resulting particles. For instance, research by Ouyang et al. demonstrated that an increased melt superheat led to a notable reduction in mean particle diameter because it allowed droplets more time to undergo breakup before solidification occurred [53]. Remarkably, secondary breakup models have not yet incorporated solidification as a variable, except for very limited studies [16], [17], [22], which motivates its inclusion as a focus of investigation in this thesis.

The treatment of solidification often involves simplifications. These include:

- Maintaining constant and uniform gas velocity and temperature
- Assuming a uniform droplet temperature throughout the solidification process.
- The gradual, non-dendritic expansion of solidification in a droplet occurs as the solidification front progresses from one side of the droplet to the other.

In the case of rapid solidification processes such as melt atomization, the solidification of melt droplets can be broken down into several stages as represented in Figure 1.13. Initially, there's the cooling phase (i), where convective and radiative heat transfer suddenly lowers the droplets' temperature to it's nucleation temperature ($T_{nuc.}$). Following this, we enter a recalescence phase (ii), during which the release of crystallization heat results in a rapid temperature increase up to the recalescence temperature (T_R), leading to the dendritic solidification of droplets. However, the melt droplets do not fully solidify during this phase.

The primary dendrites, which initially form, remain surrounded by the remaining molten material. Subsequently, crystallization occurs during the following phases (iii, iv, v), where both cooling and solidification occur concurrently. During these steps, the heat of fusion (appears in the Eutectic solidification phase iv), along with convection and radiation, leads to the transformation of the droplets from a liquid to a solid state [20, 43].

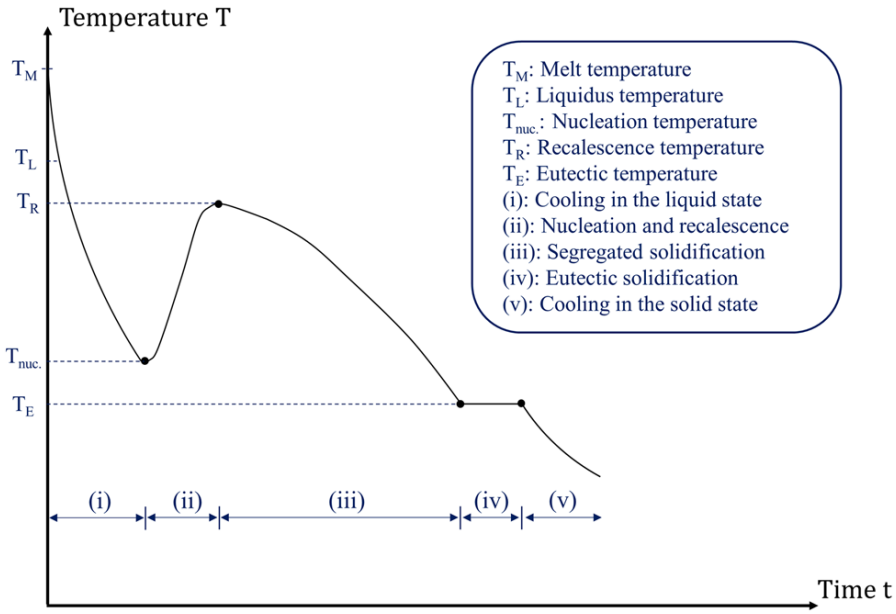

Figure 1.13: Schematic illustration of rapidly solidifying melt droplets during gas atomization [43]

Recalescence is a phenomenon characterized by a temperature increase (Figure 1.13-phase (ii)) during the solidification process. This temperature rise is a consequence of increased entropy resulting from a change in the crystal structure of the material. Recalescence is linked to the release of latent heat of fusion, which cannot be promptly dissipated by the surrounding gas phase.

As solidification begins, the heat required for crystallization is released. This heat corresponds to the same energy that was supplied during the melting process, known as latent heat. Consequently, the molten metal experiences a reheating effect due to this released crystallization heat, leading to a temperature increase, which is observed as phase (ii) on the cooling curve. Once the solidification process is complete, the temperature gradually decreases. The recalescence process concludes at Temperature T_R when the rate at which heat is dissipated by the surrounding gas becomes comparable to the rate at which latent heat is released during solidification in that phase. This equilibrium in heat exchange marks the end of the recalescence phenomenon [44, 43].

1.3 Research objectives

The research question that this thesis aims to solve is how to address the lack of solidification modeling and verify its results. To accomplish this, the approach involves initially calibrating a model specifically for secondary breakup phenomena. Subsequently, a model for solidification will be introduced, and its impact on powder properties will be investigated, comparing the results to those of non-solidified droplets.

In the next chapter, the equations governing both the TAB and KH models, along with the motion of spherical droplets characterized by a dynamic drag coefficient, will be thoroughly explored. Following that, a review of existing literature related to the equations governing the solidification of droplets will be conducted.

In the third chapter, we will implement a secondary breakup atomization model, which has been adopted from a reference paper by Liu et al. In this paper, the phenomenon was examined utilizing the KH and TAB models, and validation was carried out through experimental means. Our goal will be to apply this model and verify its performance against both the reference model and experimental data.

The subsequent chapter will witness the development of a model for the solidification of secondary breakup droplets as literature lacks solidification as a variable to the breakup models, making it a compelling focus of exploration in this thesis. Given the absence of sufficient data for solid state in Liu et al.'s paper for the Benz, iron, a material with abundant data in the literature, will be chosen.

For modeling purposes, the open-source software OpenFOAM's Lagrangian library will be employed. While an existing particle class is originally designed for breakup models, it will be modified to handle solidification. This modification will enable the simulation of both secondary breakup and solidification processes with iron, and the accuracy of our model will be validated through verification.

Chapter 2

Methodology

2.1 Software outline

2.1.1 OpenFOAM

The thesis employs OpenFOAM, an open-source software package, for simulations. OpenFOAM primarily functions as a C++ library, producing executables known as "applications." These encompass solvers for specific continuum mechanics problems and utilities for data manipulation tasks. Users can create additional solvers and utilities with appropriate knowledge. OpenFOAM includes pre- and post-processing capabilities, using its own utilities to ensure consistent data handling. Figure 2.1 outlines the software's structure.

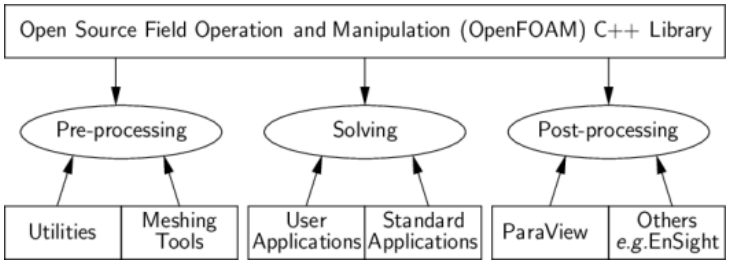

Figure 2.1: Overview of OpenFOAM structure

2.1.2 CFD Solver

The sprayFoam solver in OpenFOAM is a valuable tool for simulating atomization and droplet breakup. It employs an approach known as the Eulerian-Lagrangian method. In this method, the continuous phase (gas) is typically simulated using Eulerian methods, while the dispersed phase (spray particles or droplets) is tracked

individually using Lagrangian techniques. This allows sprayFoam to capture the behavior of the dispersed phase in a gas medium without explicitly tracking the interface between the two phases.

Unfortunately, there currently is no dedicated solver for modeling solidification and breakup phenomena simultaneously. However, within the same Lagrangian library, other solvers (e.g. those using Reacting cloud Module) capable of handling solid particles are available. A new class module can be integrated with sprayFoam for simulating solidifying sprays.

2.2 Governing Equations

As previously discussed, the mentioned dimensionless numbers (Weber, Ohnesorge, Density ratio) are limited to describe the conditions of the droplets at impact. Hence, the inclusion of phenomenological models, such as Taylor-analogy breakup (TAB) and Kelvin-Helmholtz (KH), is necessary for a comprehensive examination of the breakup dynamics. It is also necessary to account for the effects of drop oscillation and distortion on the drop drag coefficient. The model uses the approach of the TAB model to estimate the distortion of drops in a high relative velocity flow. In this section, our focus is directed towards discussing these models and their corresponding governing equations.

2.2.1 TAB model

Here we explore the Taylor-analogy breakup (TAB) concept as it applies to low Weber number conditions (We<80) for Bag and Multimode breakup modes. As shown in the Figure 2.2, this analogy draws parallels between surface tension (akin to a spring's cohesive force), external forces (resembling dynamic forces from aerodynamics), and droplet viscosity (comparable to spring-damper system). It offers an intuitive representation of the relationships between these factors in droplet breakup dynamics.

The Equation 2.1 simply shows the damped, forced harmonic oscillator:

$$F(t) = m \cdot \ddot{x} + d \cdot \dot{x} + k \cdot x \tag{2.1}$$

Where m represents the droplet mass, F denotes the (aerodynamic) force, k corresponds to the spring constant (surface tension), and d signifies the damping constant (viscosity of the droplet). By considering the analogous, m, c, and k can be written the way in Equation 2.2 in terms of the coefficients C_F, C_k, and C_d (found by O'Rourke and Amsden [39]) along with the given physical parameters ρ_l, ρ_g, a, σ, and μ_l.

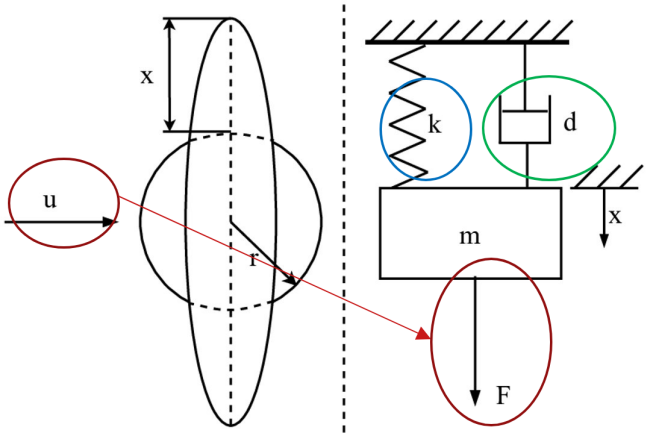

Figure 2.2: Analogical Representation of Droplet Breakup Forces on a Taylor Spring-Mass-Damper System [45]

$$\frac{F}{m} = \frac{C_F}{C_b}\left(\frac{\rho_g W^2}{\rho_l a}\right), \quad \frac{k}{m} = C_k\left(\frac{\sigma}{\rho_l a^3}\right), \quad \frac{d}{m} = C_d\left(\frac{\mu_l}{\rho_l a^2}\right) \tag{2.2}$$

Here W is constant relative velocity between the drop and the gas. By substituting these values into Equation 2.1, transforms into Equation 2.3, which signifies the oscillation of the droplet diameter.

$$\ddot{y} = \frac{C_F}{C_b}\left(\frac{\rho_g W^2}{\rho_l a^2}\right) - C_k\frac{\sigma}{\rho_l a^3}y - C_d\frac{\mu_l}{\rho_l a^2}\dot{y} \tag{2.3}$$

The distortion parameter y is called the "Level of Distortion". It is the normalized value of x, where x is the displacement of the equator of the drop from its equilibrium position as in Equation 2.4:

$$y = \frac{x}{C_b a} \tag{2.4}$$

In the implementation of O'Rourke and Amsden, breakup occurs if and only if $y > 1$ [39]. By solving the differential Equation 2.3, Equation 2.5 will be derived. This is the time history of the Level of Distortion, y.

$$\begin{aligned} y(t) = {} & \frac{C_F}{C_k C_b}We + \left[\exp\left(-\frac{t}{t_d}\right)\right] \cdot \\ & \left[\left(y_0 - \frac{C_F}{C_k C_b}\right)\cos(\omega t) + \frac{1}{\omega}\left(\dot{y}_0 + \frac{y_0 - \frac{C_F}{C_k C_b}We}{t_d}\right)\sin(\omega t)\right] \end{aligned} \tag{2.5}$$

where y_0 and $\dot{y}_0$ represent initial displacement and velocity of the droplet oscillation, respectively, and the parameters

$$We = \frac{\rho_a W^2 r}{\sigma}, \quad \frac{1}{t_d} = \frac{C_d \mu_l}{2\rho_l r^2}, \quad \omega^2 = C_k \frac{\sigma}{\rho_l r^3} - \frac{1}{{t_d}^2}, \tag{2.6}$$

where W is the relative velocity, t_d is the damping time, ω is the oscillation frequency, μ_l is the liquid viscosity, ρ_l is the liquid density. In TAB model, the initial deforming rate is related to another model parameter Amp0 in the Equation 2.7.

$$\dot{y} = \mathrm{Amp}\,0 \cdot \omega_0, \tag{2.7}$$

where ω_0 is the initial oscillation frequency for the droplet.With the assumption of isotropic turbulent state of the exit flow of the nozzle, this TAB method is intended to give a reasonable estimation for the model parameter amp0 [46, 47]. Combining Equations 2.4 and 2.7, we have:

$$\dot{y} = \frac{\dot{x}}{C_b r} = \mathrm{Amp}\,0 \cdot \omega_0, \tag{2.8}$$

where $r(t = 0) = a$ is the initial drop radius and $\dot{x}_0$ is the dimensional initial deforming rate of the drop surface. The TPB (turbulent primary breakup) method correlates $\dot{x}_0$ to the flux-averaged kinetic turbulent energy of the exit flow, k_0, by

$$\dot{x} = \sqrt{\frac{2}{3} k_0}. \tag{2.9}$$

The initial oscillation frequency ω_0 in Equation 2.8 is determined from Equation 2.6.

$$\omega_0 = \sqrt{C_k \frac{\sigma}{\rho_l a^3} - \left(\frac{C_d \mu_l}{2\rho_l a^2}\right)^2} \tag{2.10}$$

Substituting Equations 2.9 and 2.10 into Equation 2.8, we have

$$\mathrm{Amp}\,0 = \frac{1}{C_b a \omega_0} \cdot \dot{x} = \frac{1}{C_b a \omega_0} \cdot \sqrt{\frac{2}{3} k_0} = \frac{\sqrt{\frac{2}{3} k_0}}{C_b a \sqrt{C_k \frac{\sigma}{\rho_l a^3} - \left(\frac{C_d \mu_l}{2\rho_l a^2}\right)^2}} \tag{2.11}$$

The parameter Amp0 can be used as an indication of the turbulence intensity of the exiting flow. Higher Amp0 indicates larger spray angle and smaller droplets [48].

2.2.2 KH model

The Kelvin-Helmholtz (KH) model analyzes the breakup of droplet and the formation of child droplets using insights derived from the stability analysis of liquid jets. In this analysis, the stability of a liquid column emerging from a circular opening into a stationary, incompressible gas environment is considered. Initially, a small axisymmetric surface disturbance is introduced into the previously stable flow, leading to minor variations in pressure and velocity within both the liquid and gas phases. These fluctuations are governed by the continuity equation and the equation of motion, which are solved to derive a dispersion equation characterizing wave growth rates and wavelengths [49].

This model pertains to scenarios with We>80, signifying high Weber numbers. Under this framework, we make assumptions related to breakup times and droplet size, both of which are influenced by the fastest-growing instability wavelength—a wavelength that is a function of Weber number (We), Ohnesorge number (Oh), and the parent droplet radius. This, in turn, affects the breakup time.

The droplet starts to break up by an infinitesimal displacement at the surface level of the droplet in the form of Equation 2.12.

$$\eta = R\left(\eta_0 e^{i(kz+\omega t)}\right) \tag{2.12}$$

To derive equations for KH model, the linearized hydrodynamical equations are a good start as in Equation 2.13 [50]:

$$\begin{aligned}
&\frac{\partial U_l}{\partial z} + \frac{l}{r}\frac{\partial}{\partial r}\left(r v v_l\right) = 0 \\
&\frac{\partial U_l}{\partial t} = -\frac{l}{\rho_l}\frac{\partial p_l}{\partial z} + v_l\left\{\frac{\partial^2 U_l}{\partial L^2} + \frac{l}{r}\frac{\partial}{\partial r}\left(r\frac{\partial U_l}{\partial r}\right)\right\} \\
&\frac{\partial v_l}{\partial t} = -\frac{l}{\rho_l}\frac{\partial p_l}{\partial r} + v_l\left\{\frac{\partial^2 v_l}{\partial L^2} + \frac{\partial}{\partial r}\left(\frac{l}{r}\frac{\partial}{\partial r} r v v_l\right)\right\}
\end{aligned} \tag{2.13}$$

Where u_l, v_l, and p_l are small axisymmetric velocities and pressure of the droplet, and U is jet exit velocity (averaged over jet cross section). With the assumption that $\eta \ll a$, the kinematic, tangential stress, and normal stress equations are to the first order:

$$\begin{aligned}
&v_l = \frac{\partial \eta}{\partial t}, \quad \frac{\partial U_l}{\partial r} = -\frac{\partial v_l}{\partial z} \\
&-p_l + 2\mu_l\frac{\partial v_l}{\partial r} - \frac{\sigma}{a^2}\left(\eta + a^2\frac{\partial^2 \eta}{\partial z^2}\right) + p_g = 0
\end{aligned} \tag{2.14}$$

The inertial effects of the gas enter through the gas pressure p_g. This is found from the linearized inviscid equations of motion for the gas:

$$\begin{aligned}
&\frac{\partial U_g}{\partial z} + \frac{1}{r}\frac{\partial}{\partial r}(rv) = 0 \\
&\frac{\partial U_g}{\partial t} + U(r)\frac{\partial U_g}{\partial z} + \frac{dU}{dr}v_g = -\frac{1}{\rho_g}\frac{\partial p_g}{\partial z} \\
&\frac{\partial v_g}{dt} + U(r)\frac{\partial v_g}{\partial z} = -\frac{1}{\rho_g}\frac{\partial p_g}{\partial r}
\end{aligned} \tag{2.15}$$

Where the mean gas motion above the liquid surface is given by $U(r)$. The boundary conditions are:

$$\begin{aligned}
v_g = \frac{\partial \eta}{\partial t} + U\frac{\partial \eta}{\partial z} \quad \text{at} \quad r \cong a \\
U_g, v_g, p_g \to 0 \quad \text{as} \quad r \to \infty
\end{aligned} \tag{2.16}$$

In Figure 2.3, a schematic illustrates the Kelvin-Helmholtz instability phenomenon. This instability occurs at the surface of a cylindrical liquid jet that is penetrating into a stationary, inviscid, and incompressible gas with a relative velocity.

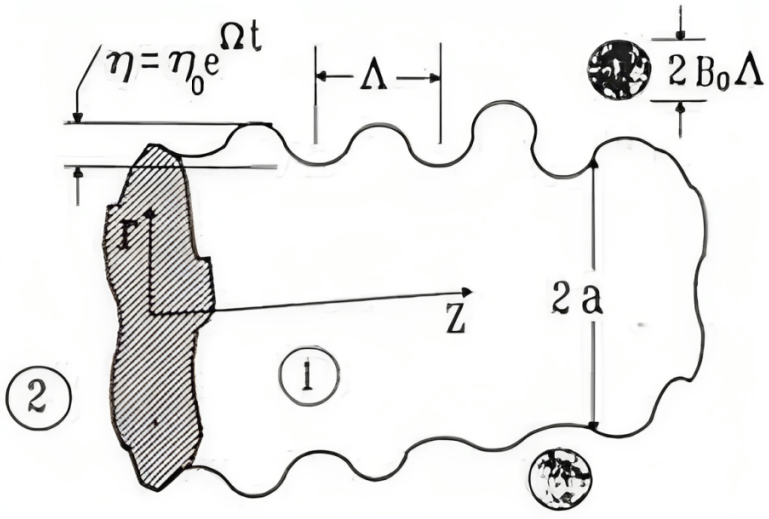

Figure 2.3: KH breakup mechanism [51]

Equation 2.13 is solved by introducing a stream function ψ_l, and a velocity potential ϕ_l and by seeking wave solutions of the form:

$$\phi_l = C_l I_0(kr)e^{i(kz+\omega t)} \tag{2.17}$$

$$\psi_l = C_g r I_l(kr)e^{i(kz+\omega t)} \tag{2.18}$$

Solutions free from singularities on the axis $r = 0$ are found to be $\Phi_l = C_l I_0(kr)$ and $\Psi_l = C_g r l_l(\ell r)$,where C_l and C_g are arbitrary constants, and the liquid pressure can then be found from the relation $p_l = -\rho_l \partial\phi_l/\partial t$.

For the gas flow, Equation 2.15 can be simplified by defining a stream function $\psi_g = (U - i\omega/k)\eta f(r)$. This leads to an Orr-Sommerfeld equation:

$$\frac{d^2 f}{dr^2} + \left(\frac{2U'r}{U - i\omega/k} - 1\right)\frac{d(I/r)}{dr} - k^2 f = 0 \tag{2.19}$$

with $f(r = a) = 1$, and $f(r \to \infty) = 0$. The equation for the gas pressure is:

$$p_g = -\rho_g \eta \left(U - i\frac{\omega}{k}\right)^2 \left(\frac{df}{dr} - \frac{r}{r}\right) \tag{2.20}$$

Here the arbitrary constant of integration has been set equal to zero. If the gas velocity profile $U(r)$ is known, the gas pressure at the jet surface can be determined from Equation 4 for use in Equation 2.14. For the special case of slip at the gas-liquid interface, $U(r) = U \equiv$ constant, and the gas surface pressure is:

$$p_g = -\rho_g \left(U - i\frac{\omega}{k}\right)^2 k\eta \frac{k_0(ka)}{k_l(ka)} \tag{2.21}$$

Finally, substituting these relationships into Equation 2.14 yields:

$$\omega^2 + 2v_l k^2 \omega \left[\frac{I_l'(ka)}{I_0(ka)} - \frac{2k\ell}{k^2 + \ell^2}\frac{I_l(ka)}{I_0(ka)}\frac{I_l'}{I_l}\frac{\ell a}{\ell a}\right] = \frac{\sigma k}{\rho_l a^2}\left(1 - k^2 a^2\right)\left(\frac{\ell^2 - k^2}{\ell^2 + k^2}\right)\frac{I_l(ka)}{I_0(ka)} + \frac{\rho_g}{\rho_l}(U - i\omega/k)^2 k^2 \left(\frac{\ell^2 - k^2}{\ell^2 + k^2}\right)\frac{I_l(ka)k_0(ka)}{I_0(ka)k_l(ka)} \tag{2.22}$$

which is the governing dispersion relationship. Equation 2.22 may for brevity be written in non-dimensional form as:

$$\beta^2 + 2Zk^2 a^2 F_l \beta = ka\left(1 - k^2 a^2\right) F_g + We_g k^2 a^2 F_3 \tag{2.23}$$

Where:

$$\beta = \omega\sqrt{\rho_l a^3/\sigma}, \quad Z \ = \mu_l/\sqrt{\rho_l \sigma d}, \quad We_g = \rho_g U^2 d/\sigma$$

and the F's are dimensionless ratios of Bessel functions and wave numbers.

For the special case $Z = 0$ and $We_g = 0$ (inviscid liquid jet at low velocity) the dispersion Equation 2.22 (cf. also Equation 2.23) becomes:

$$\omega^2 = \frac{\sigma k}{\rho_l a^2}\left(1 - k^2 a^2\right)\frac{I_l(ka)}{I_0(ka)} \tag{2.24}$$

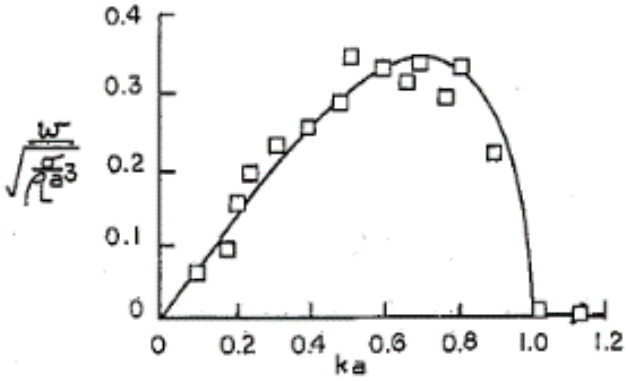

Figure 2.4: Wave growth rate with wave number for jets in Rayleigh breakup regime: line-theory Equation 2.24; Symbols-measured wave growth rates of Donnely and Glaberson [52]

This equation predicts that the jet surface is unstable for all wavenumbers with ka < 1 and the corresponding wavegrowth curve is given in Figure 2.4. This wavegrowth curve can be found experimentally by vibrating low speed jets at various frequencies and by measuring the growth rate of the axisymmetric surface oscillations. The corresponding measurements of Donnely and Glaberson [52] given in Figure 2.4 show excellent agreement with the first-order theory. Differentiating Equation 2.24 shows that the maximum growth rate is

$$\omega_m \cong 0.34 \left(\frac{\sigma}{\rho_1 a^3}\right)^{1/2} \text{ at } k \cong 2\pi/9.02a \tag{2.25}$$

Equation 2.22 can be written also in the form of Equation 2.26:

$$\begin{aligned} \omega^2 + 2v_l k^2 \omega \left(\frac{I_l'(ka)}{I_0(ka)} - \frac{2k\Lambda}{k^2+\Lambda^2}\frac{I_l(ka)}{I_0(ka)}\frac{I_l'}{I_l}\frac{ka}{ka}\right) = \\ \frac{\sigma k}{\rho_l a^2}\left(1-(ka)^2\right)\frac{k^2 a}{k^2 a}\frac{I_l(ka)K_0(ka)}{I_0(ka)K_l(ka)} \end{aligned} \tag{2.26}$$

Where:

$$\Lambda^2 = k^2 + \frac{\omega}{\nu_l}k = \frac{2\pi}{\lambda}, \quad ka < 1(\text{where } \lambda = 9.02a) \tag{2.27}$$

Where numerical solutions leads to single maximum in growth rate $\omega(=\Omega) = \frac{2\pi}{\lambda(=\Lambda)}$ [51]. So for 80 $<$ *We*$<$ 800, by substituting values from Equation 2.25 into Equation 2.26, the fastest-growing (most probable) wavelength disturbances (Λ) can be

simplified as presented in the Equation 2.28 and for maximum growth rate (Ω) in Equation 2.29.

$$\Lambda = \frac{9.02\,(1+0.45Z^{0.5})\,(1+0.4T^{0.7})}{\left(1+0.87\,We_g^{1.67}\right)^{0.6}} \cdot r \quad (r=a) \tag{2.28}$$

$$\Omega = \frac{0.34+0.38\,We_g^{1.5}}{(1+Z)(1+1.4T^{0.6})}\sqrt{\frac{\sigma}{\rho_l r^3}} \quad (r=a) \tag{2.29}$$

Where:

$$Z = Oh = \frac{We_l^{0.5}}{Re_l}, \quad T = Z\,We_g^{0.5}, \quad We_l = \frac{\rho_l W^2 a}{\sigma}$$
$$We_g = \frac{\rho_g W^2 a}{\sigma}, \quad Re_l = \frac{Wa}{\nu_l}$$

The process of liquid breakup is described by assuming the formation of new droplets with a radius, denoted as r, originating from bulk liquid or "blobs/parcels" with a characteristic radius, represented as a:

$$r = B_0\Lambda \qquad \text{if } B_0\Lambda \le a \tag{2.30a}$$

$$\text{or } r = \min\left\{ \begin{array}{l} (3\pi a^2 W/2\Omega)^{0.33} \\ (3a^2\Lambda/4)^{0.33} \end{array} \right\} \quad \text{for } (B_0\Lambda > a, \text{one time only}) \tag{2.30b}$$

Equation 2.30b applies only to low velocity liquid undergoing Rayleigh-Taylor breakup as shown in the Figure 2.5. This model considers instabilities, especially in cases involving the acceleration of small droplets by gas. It assumes that the jet disturbance has a frequency of $\Omega/2\pi$ (a drop is formed each period) or that drop size is determined from the volume of liquid contained under one surface wave.

The characteristic size of the unstable parent bulk liquid changes continuously with time called as Breakup Time:

$$t_b = \frac{3.72B_1 r}{\Lambda\Omega} \tag{2.31}$$

and B_1 is the breakup time constant [51].

2.2.3 Drop Drag Model

The equation governing the motion of a spherical droplet in a gas with respect to their relative velocity, denoted as W, is defined in Equation 2.32.

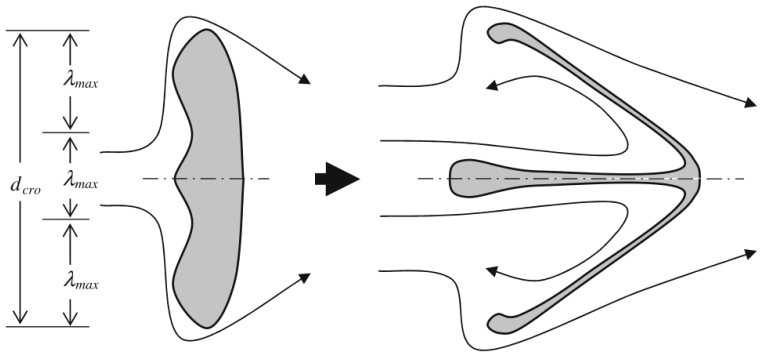

Figure 2.5: Breakup due to combined Rayleigh–Taylor (R–T)/aerodynamic drag mechanism

$$\rho_l V \frac{d^2 \bar{X}}{dt^2{}^2} = \frac{C_d A_f \rho_g W^2}{2} \tag{2.32}$$

Where X represents the droplets position vector, V its volume, C_d is drag coefficient, and A_f its frontal area. Typically, the droplet's drag coefficient (Equation 2.33) is determined based on that of a rigid sphere [53].

$$\mathrm{C}_d = \begin{cases} \frac{24}{\mathrm{Re}} \left(1 + \frac{1}{6}\mathrm{Re}^{2/3}\right), & \text{if } \mathrm{Re} \leq 1000 \\ 0.424, & \text{if } \mathrm{Re} > 1000 \end{cases} \tag{2.33}$$

However, when a liquid droplet enters a gas stream with a sufficiently high Weber number, it undergoes deformation due to interactions with the gas, as shown in Figure 2.2. In Taylor's research [54], it was proposed that a deformed liquid droplet adopts a plano-convex lenticular shape with the same volume as the original spherical droplet, mainly due to the gas stream's acceleration. This flattened droplet has a diameter approximately 3.76 times that of the original sphere. The shortcoming of this simple approach is that other important parameters, such as the liquid surface tension, viscosity, and the flow conditions, are not included, and the deformed drop has a constant shape even though the flow conditions may be changing.

At high relative velocities, the deforming liquid droplet not only changes its shape but also breaks up, making its drag coefficient dependent on both its Reynolds number and oscillation amplitude. To address this, the Taylor analogy model equation is used to predict the amplitude of surface deformation during droplet-gas interaction. Then an empirical relationship between the liquid droplet's drag coefficient and its deformation magnitude is established, serving to assess the impact of a dynamically changing drag coefficient on spray behavior.

In the computations, the droplet's surface oscillation amplitude is determined, using the TAB Equation 2.3. To represent the drag coefficient of a deforming droplet within the range bounded by a rigid sphere's lower limit (Eq. 2.33) and a disk's upper limit (1.52), a simplified expression in Equation 2.34 is employed.

$$C_d = C_{d,\text{sphere}}(1 + 2.632y) \tag{2.34}$$

where y represents the drop distortion calculated using the TAB model (Eq. 2.3). This equation bridges the gap between the drag coefficients of a rigid sphere and a disk, with no distortion (y = 0) approaching that of a rigid sphere and maximum distortion (y = 1) approaching that of a disk.

2.2.4 Solidification

As described in the section 1.2.7, rapid solidification of droplets in atomizer undergoes five phases, including liquid-phase cooling, recalescence, segregated solidification, peritectic solidification, and solid cooling [55]. In the model introduced by Hu et al., as depicted in Figure 2.6, the scenario illustrates the formation of the initial nucleus on the droplet surface, growing along the droplet diameter. Assuming constant curvature of the nucleus, the percentage of the solid phase during the growth process can be expressed as follows in the Equation 2.35 [55, 56]:

$$f_s = \frac{3d_p x^2 - x^3}{2} \tag{2.35}$$

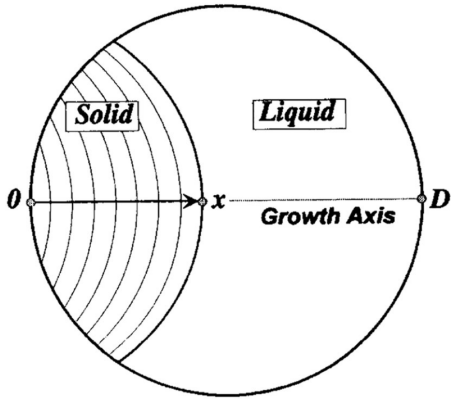

Figure 2.6: Schematic of single nucleation on the droplet surface. [55]

The heat conservation equation can be described by [56]:

$$\frac{dT_d}{dt}\left(c_d + \Delta h_f \frac{df_s}{dT_d}\right) = -\frac{6h}{\rho_d d_d}(T_d - T_g) - \frac{6\varepsilon\sigma}{\rho_d d_d}\left(T_d^4 - T_w^4\right) \tag{2.36}$$

with f_s as fraction solid ($f_s = 0$: droplet is completely liquid; $f_s = 1$: droplet is completely solid). In the Equation 2.36 T_d is the droplet temperature, T_g the gas temperature, and T_w the temperature of the surrounding walls. The specific heat capacity of the liquid droplet material is $c_{d,l}$, h is the heat transfer coefficient, ϵ and σ are the emissivity and Stefan–Boltzmann constant, ρ_d and d_d are the droplet's density and diameter, respectively. The specific heat capacity of the droplet c_d as the average of the solid and liquid content:

$$c_d = f_s c_{ds} + (1 - f_s)\, c_{dl} \tag{2.37}$$

where the solidification kinetics can be expressed as:

$$\frac{df_s}{dt} = \frac{df_s}{dx}\frac{dx}{dt} \tag{2.38}$$

which then leads to:

$$\frac{df_s}{dx} = \frac{1}{d_p}\left(3\left(\frac{x}{d_p}\right) - \frac{3}{2}\left(\frac{x}{d_p}\right)^2\right) \tag{2.39}$$

By approximating the velocity of the solid–liquid interface movement as a linear crystal growth rate function of undercooling we get:

$$\frac{dx}{dt} = K_{sl}\left[T\left(f_s\right) - T_p\right] = K_{sl}\Delta T \tag{2.40}$$

K_{sl} is the solid–liquid interfacial mobility, having a magnitude of 0.01 $m.s^{-1}.K^{-1}$. Finally by considering the Scheil's equation we can write:

$$\frac{df_s}{dT_d} = \frac{1 - f_{s,r}}{\left(k_e - 1\right)\left(T_M - T_{d,r}\right)}\left(\frac{T_M - T_d}{T_M - T_{d,r}}\right)^{(2+k_e)/(k_e-1)} \tag{2.41}$$

with T_M as liquidus temperature of pure solvent substance (base material), k_e is the equilibrium partition ratio, and $T_{d,r}$ and $f_{s,r}$ as the solid fraction and temperature of the droplet after recalescence, respectively. For each phase, certain simplifications are applicable; for instance, during recalescence, $T_d = T_r$, where T_r represents the constant recalescence temperature. Similarly, after the solid fraction reaches $f_s = 1$, the term df_s becomes null.

Models implemented by Bergmann et al. [56] showed that unlike droplets moving in the core region of the spray, the temperature of droplets within the edge region of the spray cone decreases much faster and earlier since they are in direct contact with the colder ambient gas. Their finding also shows that smaller droplets (10 μm) cool faster and exhibit larger and rather sharper recalescence. Whereas whole solidification process of the bigger droplets (120 μm) takes more time and recalescence happens later in their flight distance.

Since the present study involves modeling a single droplet, the cooling behavior will resemble the droplet on the edge. If solidification occurs near the breakup limit (when breakup stops) and the droplet is adequately small, it is reasonable to assume that early stages of solidification during recalescence (roughly 30-50% [56]) can take place within a few modeling steps during flight time (roughly 1.5e-04 seconds). Since breakup only occurs in the liquid phase, the dimensions of the liquid fraction are considered for calculation of the breakup. Consequently, the gas Weber number falls below the critical value, and the droplet no longer undergoes breakup, even though the total diameter of drop is still high. In this scenario, as an initial step towards simulating solidification, it is justifiable to model this phenomenon by changing the phase of the droplet in a single step.

2.3 Model setup

This section provides the information of the general setup as outlined in the model introduced by Liu et al. [1]. Experiments of liquid drop breakup done by Liu et al. [1] were carried out in an apparatus that consisted of a drop generator and an air nozzle with a converging exit, arranged in a cross-flow pattern, as shown in Fig. 2.7 [10]. The monodisperse stream of liquid drops was generated by a Berglund-Liu drop generator [11]. In the figure, it is evident that droplets are introduced on the left side of the air stream, while the air flows downward.

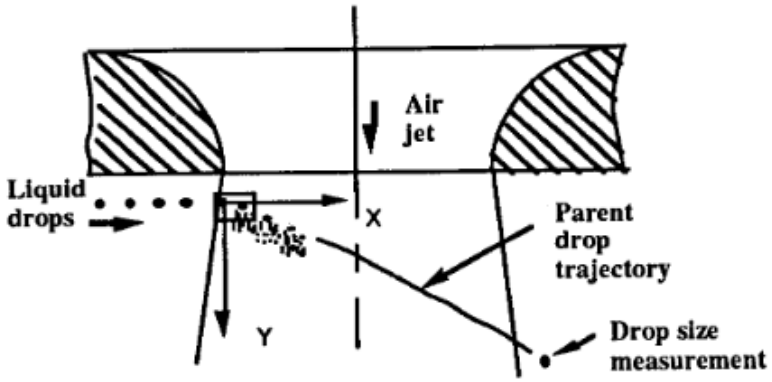

Figure 2.7: Illustration of the experimental setup featuring a coordinate system, trajectory, and drop size measurements. A uniform liquid drop stream, with a diameter of 170 µm, is introduced into a transverse air jet, resulting in its disintegration. [1]

Model specifications are summarized in Table 2.1. The computational domain consists of a cylinder with dimensions of 52 mm in diameter and 57 mm in length. Inside the cylinder, a mesh configuration of $32 \times 16 \times 84$ is utilized. The air nozzle, positioned vertically from the top, initiates a jet with zero initial velocity, influenced

solely by gravity. This jet is emitted from a nozzle with a diameter of 9.525 mm (R/D=0.5). The gas velocity is gradually increased to a steady state. The droplets, consisting of Benz UCF-I fuel, conforming to SAE J967d specifications, have a diameter of 170 µm. They are ejected from the fuel nozzle at a velocity of 16 m/s, with the nozzle positioned horizontally at the edge of the jet and 2 mm downstream of the air nozzle exit plane, facilitating the injection process. The fuel nozzle operates at a frequency of 4×10^4 parcels per second, with the same exit diameter as that of the droplets diameter.

Model Specifications		
Cylinder	Diameter × Length	52 × 57 (mm)
	Mesh	32 × 16 × 84 (Ra × Az × Ax)
Air Nozzle	Position	Vertical from Top
	Jet Initial Velocity	0
	Diameter (R/D=0.5)	9.525 mm
Droplet	Diameter	170 µm
Fuel	Benz UCF-I	SAE J967d
	Specifications	
	Density	824 kg/m^3
	Dynamic Viscosity	2.17×10^{-3} Pa.s
	Surface Tension Coefficient	0.02 kg/s^2
Fuel Nozzle	Horizontal Position	4.7625 mm from the jet axis
	Vertical Position	2 mm downstream of the air nozzle exit plane
	Direction	Horizontal
	Injection Specifications	
	Injection Frequency	4×10^4 Parcel/s
	Exit Diameter	170 µm
	Injection Velocity	16 m/s

Table 2.1: Model specifications

2.3.1 KH Setup

Selecting the suitable constants for Equation 2.30 holds significant importance. The selection of the constant $B_0 = 0.6$ is deliberate, chosen to align with experimental

data concerning stable drop sizes in sprays [51]. B_1, the breakup time constant, is recommended as $B_1 = \sqrt{(3)}$ by O'Rourke and Amsden [39]. In the context of high-speed drop breakup, Ranger and Nicholls' [57] data suggests $B_1 = 8$, while in engine spray modeling studies, Reitz [51, 58] used $B_1 = 10$. This discrepancy highlights uncertainty regarding the appropriate constant value. This uncertainty may partly arise from prior analyses neglecting drop acceleration after entering high-velocity gas flows. Such acceleration leads to longer wavelengths and breakup times, a phenomenon accounted for in the current study by including drop acceleration calculations in the model. Computational results are sensitive to the breakup time proportionality constant in wave and TAB models. However, it is crucial to understand that using the same constant value can still yield different breakup rates due to variations in the models' physics and implementations.

As discussed in the governing equations, the distorsion parameter (y) is a component of the TAB model, and its analogy applies exclusively to the drop drag model. To incorporate this analogy into the oscillation equation while using the KH model in OpenFOAM, the same TAB model coefficient can be introduced to KH model to account for droplet oscillation.

2.3.2 TAB Setup

Equation 2.3 can be analytically solved for a constant relative velocity, W, between the droplet and the gas. The constants C_F, C_k, C_d, and C_b have been determined by O'Rourke and Amsden [39] through a comparison of experimental and theoretical outcomes, yielding the following values: $C_k = C_\omega = 8$, $C_F = 1/3$, $C_d = C_\mu = 5$, and $C_b = 1/2$. For more comprehensive information, refer to O'Rourke and Amsden [39]. In OpenFOAM, C_F and C_b have been replaced by a new parameter called the Critical Weber number, which is determined using the equation 2.42:

$$We_{cr} = \frac{C_\omega \cdot C_b}{2 \cdot C_F} = \frac{8 \cdot 1/2}{2 \cdot 1/3} = 6 \tag{2.42}$$

These constant values imply that the breakup time constant, B_1, would be equal to $\sqrt{\frac{1}{C_F}} = \sqrt{3} = 1.73$ for high Weber numbers and inviscid liquids [51].

Chapter 3

Secondary breakup Modelling

As discussed in the research objectives preceding the modeling of droplet solidification, it is valuable to first calibrate and validate a breakup model for non-solidified droplets using experimental results. Subsequently, the focus can shift towards modeling the process of solidification. To do so, this chapter exclusively focuses on the validation of the secondary breakup phenomena as outlined in the model introduced by Liu et al. [1]. The decision to select this paper is motivated by their comprehensive description of both experimental and simulation methodologies. The experimental findings by Liu and Reitz [10] are then employed to validate the secondary breakup model, utilizing both the TAB and Wave breakup models. The wave model introduced in the paper corresponds to the Kelvin-Helmholtz (KH) model.

3.1 Model setup

Model specifications are summarized in Table 2.1. The fuel droplets consist of Benz UCF-I fuel. The experiments were performed in atmospheric air at room temperature to avoid vaporization effects. The air jet (vertically downward) velocity was varied between 0 and 250 m/s. In this implementation only 3 out of 9 discussed cases considered in the experiments will be modelled as summarized in the table 3.1.

Case	Air Velocity (m/s)	We	Re	Breakup Regime
2	59	36	669	Bag
3	72	53	816	Bag
4	100	102	1133	Bag

Table 3.1: Experimental conditions and results used by Liu et al. [[1]]

3.2 Methodology

In both simulation and experiments introduced by Liu et al. [1], a steady airflow with a flat, continuous profile enters at the inlet. The Phase Doppler Particle Analyzer (PDPA) described in their paper is the method employed to extract droplet characteristics. PDPA functions by emitting two coherent laser beams of identical wavelength. When these lasers intersect, they create an interference pattern through the constructive and destructive interference of the two beams, resulting in a well-defined interference wave frequency. When a droplet passes through this interference pattern, it acts as a prism, causing the pattern to refract. The receiver unit of the phase Doppler instrument detects this refracted pattern and analyzes it to extract valuable information about the droplet's characteristics. a schematic of PDPA is shown in the figure 3.1.

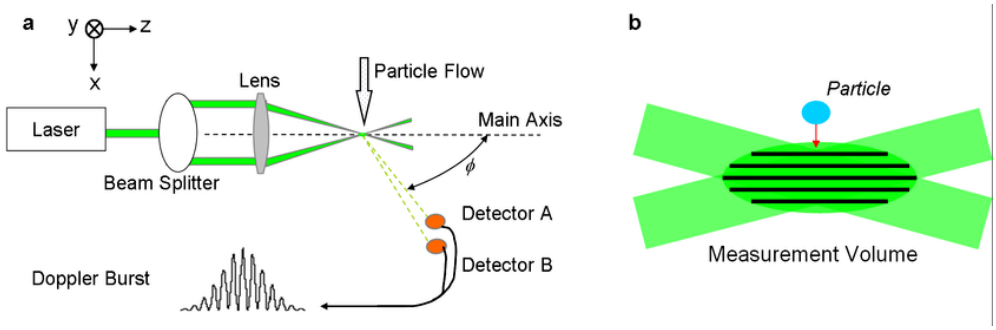

Figure 3.1: 1: Schematic of basic operating principle of PDPA.[59]

To match the velocities from Liu et al.'s paper [1], a gradual increment in velocity per time step is employed to ensure continuity error-free simulations. This increment is achieved using OpenFOAM's `#codeStream` feature, allowing for time and location-dependent customization of conditions. The droplet's position for Case 2 is depicted in the figure 3.2, where it is represented in white and observed at the left edge of the nozzle. This injection of the droplet occurs when the velocity field is fully developed.

In the initial step, the focus lies on determining the Reynolds number of a single

Figure 3.2: Visualizing the airflow and droplet injection location for Case 2.

droplet and the diameter of the parent droplet at the point of breakup for Case 4. Subsequently, in the second phase, we calculate the Sauter Mean Diameter (SMD) for both Case 2 and Case 3 to assess and compare both TAB and KH models. Only in these two cases droplets successfully reached the other side of the air stream. Finally, we track the trajectories of the droplets for cases 2 and Case 4, not only to comprehend the breakup mechanism but also to assess the influence of the drag model on droplet motion. All data has been extracted and regenerated by point picking from the diagrams presented in Liu et al.'s paper.

3.3 Validation & Results

Specifically, for atomization, the OpenFOAM solver named "sprayFoam" is embedded to the software, capable of handling breakup models like TAB and ReitzKH-RT. The latter has been adapted to align with the wave model introduced by Liu et al. Additionally, proper setup for coefficients has been established for both TAB and KH, including the capability to calculate dynamic drop drag models and solve oscillation equation for both models, as well as proper injection specifications for both air jet and fuel nozzles.

3.3.1 Drop Breakup

The Reynolds number and the diameter of the parent droplet are assessed as they progress along the horizontal penetration distance into the air stream. The outcomes for the Reynolds number and droplet diameter are visually represented in Figures 3.3 and 3.4, respectively. The original Reynolds number and droplet diameter from the paper are depicted by green line and dashed blue line respectively.

In the same graphs, our current study's results are shown with blue lines for KH and orange lines for TAB. It's important to note that the horizontal penetration distance in the figures starts at -4.7625 mm (half an air nozzle diameter), matching the injection location in the simulation.

In Figure 3.3, a rise in the Reynolds number behavior is evident for all cases, more evident in TAB model, upon droplet injection at the air stream's edge, signifying the sudden velocity change of the droplet due to being entrained by gas jet having large velocity. In the current KH simulation, the decrease in diameter comes to a halt earlier than the data from Liu et al., despite exhibiting the same shift. As the droplet moves further into the air stream, the Reynolds number gradually decreases because the droplet accelerates downstream, leading to a reduction in relative velocity used in Re calculation (Equation 1.2), and subsequently, a decrease in Reynolds number (Re). Fluctuations appearing in the paper's results are attributed to the presence of gas turbulence. In the TAB model, Re initially spikes to higher level (due to the droplet injection), but then quickly drops, indicating rapid breakup caused by the initial velocity's distortion of the parent droplet and swift formation of child droplets. This early formation of child droplets results in a lower relative velocity compared to other models because the droplet acceleration is larger. Consequently, the Reynolds number remains lower than that of KH and wave models.

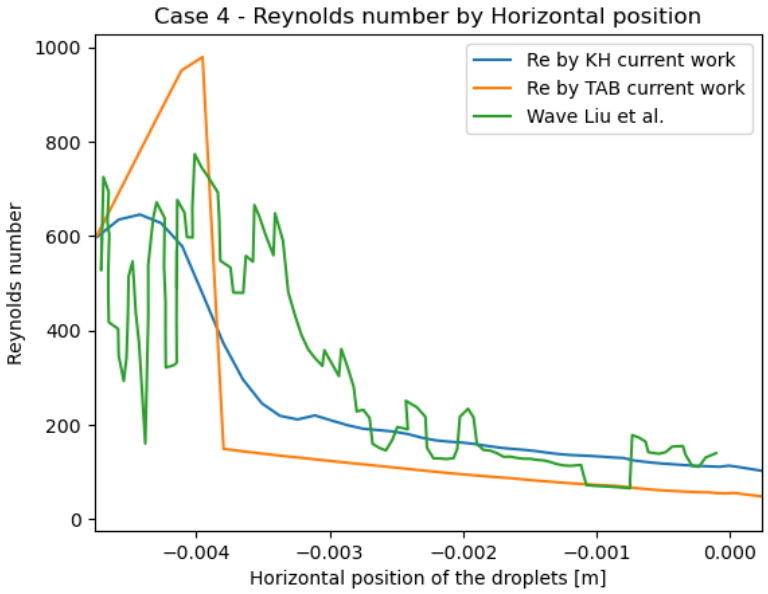

Figure 3.3: Reynolds number variation along horizontal penetration distance for Case 4.

Figure 3.4 depicts the droplet diameter in Case 4 as the parcel penetrates the

jet. The blue dashed line shows the Wave model results as a reference by Liu et al., where the droplet size steadily decreases upon entering the airflow, until it travels approximately 2 mm within the air stream. This decrease in droplet size, depicted in the numerator of Equation 2.42, leads to a reduced Weber number. If the diameter reaches a level below the critical Weber number ($We_{cr} = 6$), breakup does not happen, and the diameter remains constant beyond the 2 mm mark (where breakup no longer happens). In the current implementation of KH model, the breakup begins earlier than in Liu et al.'s work, observed in both the solid blue line (using dynamic drag coefficient) and the dotted green line (using standard drag coefficient). The reason is that the variation of We_g in the paper is close to We_{cr} at the time of injection, occasionally dropping below the critical value before reaching fully developed velocity. This particularly stems from poorly described setup condition for gas jet edge, but the breakup slope at the first half of the Figure 3.4 matches the slope related to reference data, justifying similar breakup behaviour. Ultimately, the final droplet diameter for KH reaches a similar value (the value is much closer to standard drag model than the dynamic one probably because standard drag coefficient is used for calculation of diameter in the breakup model used by Liu et al.). In the TAB model, represented by the orange line, the breakup process initially takes more time for the first droplet to break up. However, once it does, it rapidly disintegrates into child droplets. As previously discussed in the context of the Reynolds number graph, TAB tends to underestimate the final droplet size when compared to measured data.

In both results from Figure 3.4, there's a notable decrease in droplet diameter upon entering the air stream. While the exact distance of this decrease varies, both models reach a final droplet diameter of around 40 μm. This indicates that the conditions for KH-instability and breakup equations are no longer met, which relates to the Weber number of the liquid. As the droplet diameter decreases during breakup, both the Reynolds and Weber numbers follow a similar trend. This reduction in Weber number limits disturbance growth, preventing further breakup.

3.3.2 Sauter Mean Diameter

Figures 3.5 for Case 2 and 3.6 for Case 3, present variation in drop Sauter mean diameter over residence time in the air jet for TAB (orange color) and KH (blue color) model for the current simulation (solid lines), the paper's simulation (dashed lines), and the experiment (solid black circle). For both cases, the dynamic drag (DD) model described in section 2.2.3, is used to calculate forces on the droplet. Additionally, standard drag results for KH models have been shown by dotted green lines to compare.

According to Figure 3.5, the computed drop diameters, using the wave breakup model (Liu et al.) with blue dashed line (with $B_1 = 1.73$), align remarkably well

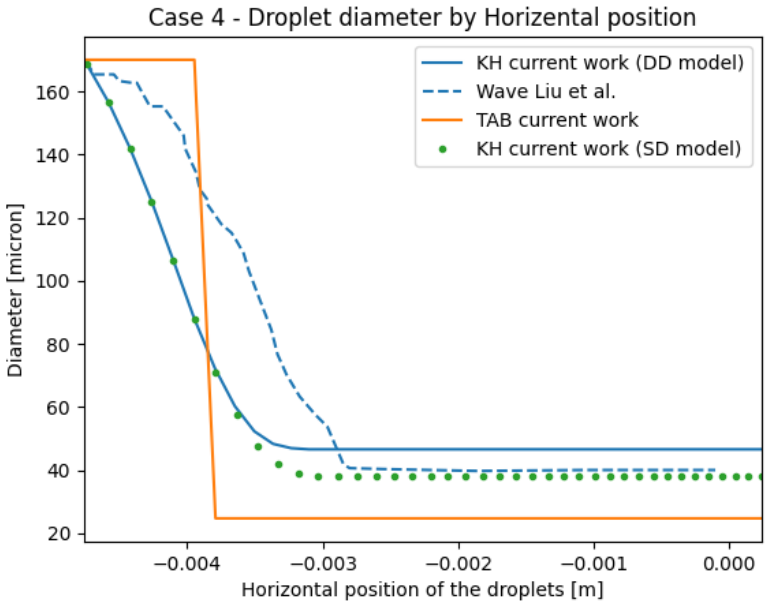

Figure 3.4: Parent droplet diameter evolution for Case 4. [DD: Dynamic Drag, SD: Standard Drag] ($We_g \approx 18_{@\ injection\ w/\ KH}$)

with the PDPA measurement. The drop size comparison for KH model validates the effectiveness of the results from the combined KH breakup and standard drag models.

For the KH model, Liu et al.'s data indicates a rather fast reduction in droplet diameter upon injection into the air stream, attributed to a sudden increase in relative velocity proportional to Reynolds number (Re). Contrary to these findings, our current research reveals that droplet breakup initiates even faster than reported in the literature.

As discussed earlier in chapter 2, the breakup time and child droplet radius exhibit a strong dependency on the Weber number of the surrounding gas, which, in turn, is contingent on the relative velocity between the gas and the droplet. Breakup occurs only when the Weber number of the gas exceeds a critical value (e.g., 6). In Liu et al.'s paper, the injection position is described, and the gas profile is defined as flat. However, as the gas regime is developed, the boundary conditions defines the edge velocity profile, and the position of the injection might have different properties. In our cases, the edge of the gas jet is defined where the gas speed is approximately half of the maximum speed, leading to different breakup behavior compared to the observations in Liu et al.'s work.

The reduction in Sauter mean diameter (SMD) stops earlier in current work results compared to the one presented in the paper, possibly due to the adjustment

of initial oscillation of the droplet introduced in dynamic drag model. Comparing Liu et al.'s simulation with the experiment, the Sauter mean diameter (SMD) outside the air stream closely matches experimental data upon introducing standard drag model as shown with green dotted line. On the contrary, utilizing dynamic drag model results in higher final SMD.

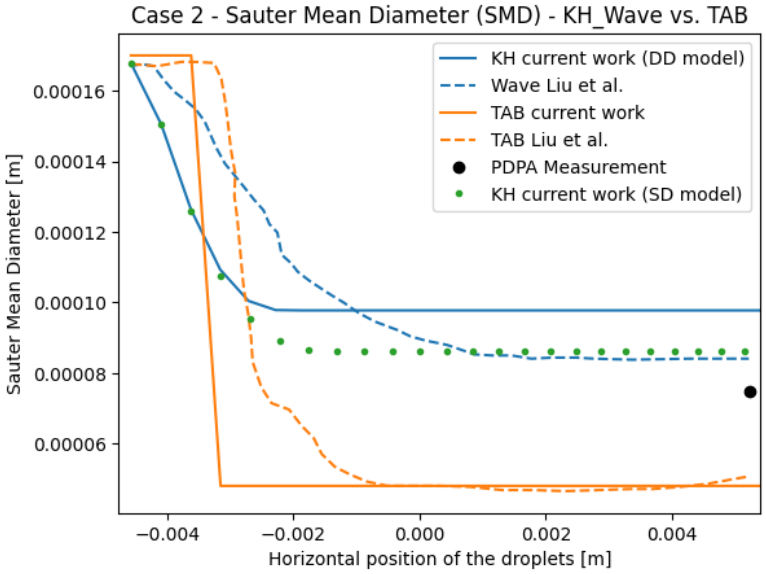

Figure 3.5: Sauter mean diameter results for TAB and KH models in Case 2, Solid circle shows PDPA measured drop diameter outside air jet. [DD: Dynamic Drag, SD: Standard Drag] ($We_g \approx 7.2_{@\ injection\ w/\ KH}$)

As discussed in the previous section for Case 4, Sauter mean diameter (SMD) values in the TAB model rapidly decrease to levels significantly below the experimental results (converges to a SMD <60 μm for Case 2), indicating poor accuracy in predicting the final breakup diameter for parent droplets. This discrepancy is attributed to the fast breakup mechanism as droplets enter the model. The TAB model proved relatively insensitive to the drop drag coefficient at high gas velocities. In this regime, the distortion parameter (y) quickly reached its maximum value, causing rapid parent drop breakup into smaller drops, which rapidly matched the gas velocity.

One consequence of the absence of surviving parent drops in the TAB model is an underestimation of the final drop size compared to the wave model. The TAB model consistently underestimated the measured final drop sizes, suggesting an overestimation of breakup effects. However, in the current work, the TAB model aligns well with the TAB model presented by Liu et al, but not with experimental. On the other hand, the breakup of the droplet over KH simulation matches better

with experiment than the TAB simulation does. This shows the accuracy of KH over TAB in predicting breakup diameters.

Based on Figure 3.6, a similar trend to Case 2 can be observed in Case 3. The main difference is that the final breakup occurs slightly earlier compared to the paper's implementation. The KH model closely follows the reference data and aligns slightly better with Case 3 than with Case 2. Indeed, the final Sauter mean diameter (SMD) results obtained by employing the dynamic drag model align well with those presented in the paper. However, when the standard drag is utilized for KH breakup diameter, we achieve a perfect match with experimental results. It is evident that the final breakup diameter in Case 3 is approximately 20 μm smaller than in Case 2 for both TAB and KH. This difference is attributed to the higher air jet velocity, which increases the relative velocity between the gas and the droplet.

Upon comparing the three cases (2, 3, and 4), the 10 μm difference is evident between the final parent diameter prediction using the dynamic drag model over the standard one which justifies the accuracy of the latter one when computing diameters.

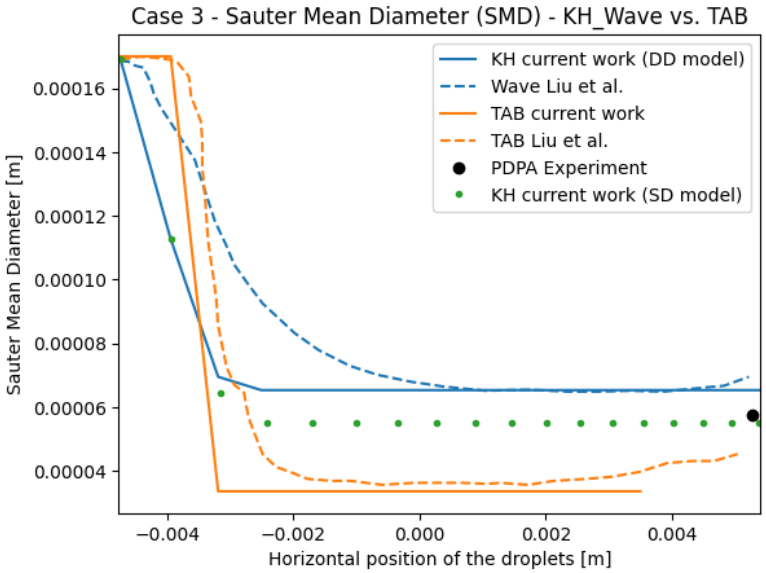

Figure 3.6: Sauter mean diameter results for TAB and KH models in Case 3, Solid circle shows PDPA measured drop diameter outside air jet. [DD: Dynamic Drag, SD: Standard Drag] ($We_g \approx 11$ *@ injection w/ KH*)

3.3.3 Trajectories

In Cases 2 and 4, we conducted trajectory measurements to compare experiments, computational models, and reference data. In the Liu's paper, drop size measurements were only possible at low air velocities when liquid drops could penetrate through the opposite side of the air jet. In these cases, we compared the measured drop Trajectories, specifically those of the longest-penetrating drops (parent drops), with computational results from both our current work and that of Liu et al.

Case 2

For the KH model, as shown in the Figure 3.7, the Dynamically varying drop drag coefficient reported to produced better results than the standard rigid sphere drag coefficient model, particularly when using the breakup time constant $B_1 = 1.73$. Higher B_1 values yielded poorer agreement with experiments [1]. It was noted that adjusting the drop breakup time constant alone, without increasing the drag coefficient value beyond the rigid sphere value, could not simultaneously match measured trajectory and final drop size. However, as demonstrated in Figure 3.7, using the dynamic drag coefficient (with $B_1 = 1.73$) provided satisfactory agreement with both experimental and Liu et al.'s simulation measured trajectories, highlighting the drag model's impact, especially at low gas velocities.

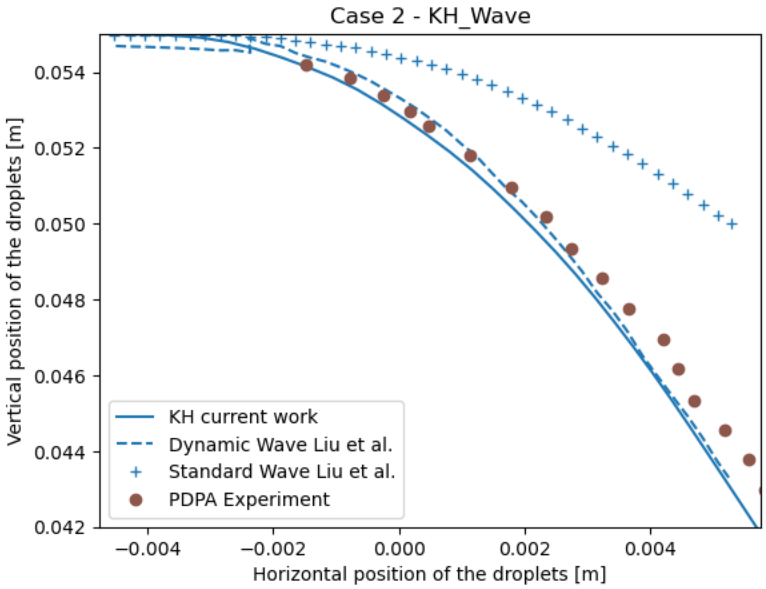

Figure 3.7: Trajectory results from the and KH-model for the current work and reference data in Case 2.

For the TAB model, excellent agreement with measured data presented in the

Figure 3.8 was observed in Case 2 (air velocity 59 m/s) when the initial oscillation parameter (Amp0) was set to zero (to comply with the injection in experiment). Varying Amp0 showed that Amp0=0 was the most suitable choice. However, increasing Amp0 led to significant deviations from measured data.

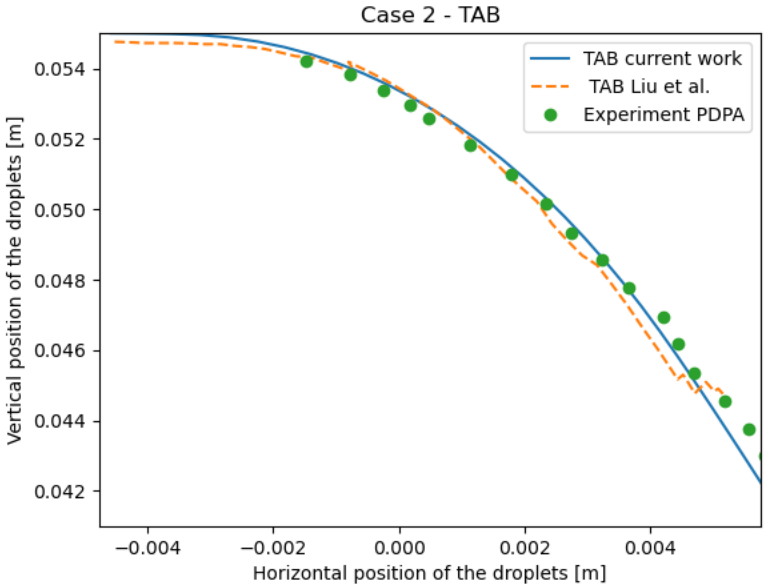

Figure 3.8: Trajectory results from the and TAB-model for the current work and reference data in Case 2.

Case 4

Utilizing the same method as described in Case 2, fair results were obtained for Case 4 with a higher air jet velocity. However, according to the Figure 3.9 a small deviation between the results and those of the paper becomes noticeable after the droplet penetrates into the jet for both KH, occurring around 3 mm into the jet. Noticeably, the simulation matches the PDPA experiment even better than the papers one in the first half. Looking at the Figure 3.10, the deviation can be observed from the same point on the horizontal axis onward. However it is evident that after a certain amount of penetration this deviation starts to get smaller.

One reason for such misalignment to the fluctuation depicted in the Figure 3.10 could be that the method used to track the blob differs from the one employed by the paper. Another possibility could be that utilizing parcels for all droplets generated from the breakup process of the parent droplet affects the precise trajectory measurements.

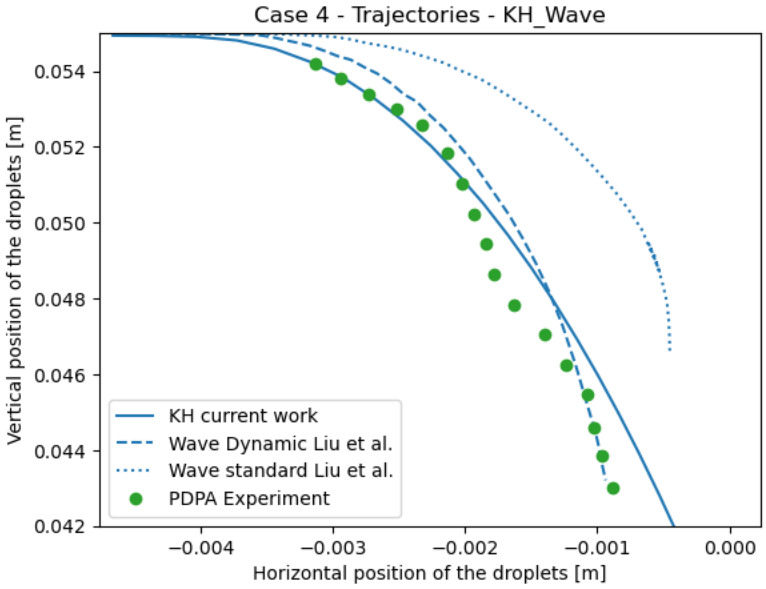

Figure 3.9: Trajectory results from the and KH-model for the current work and reference data in Case 4.

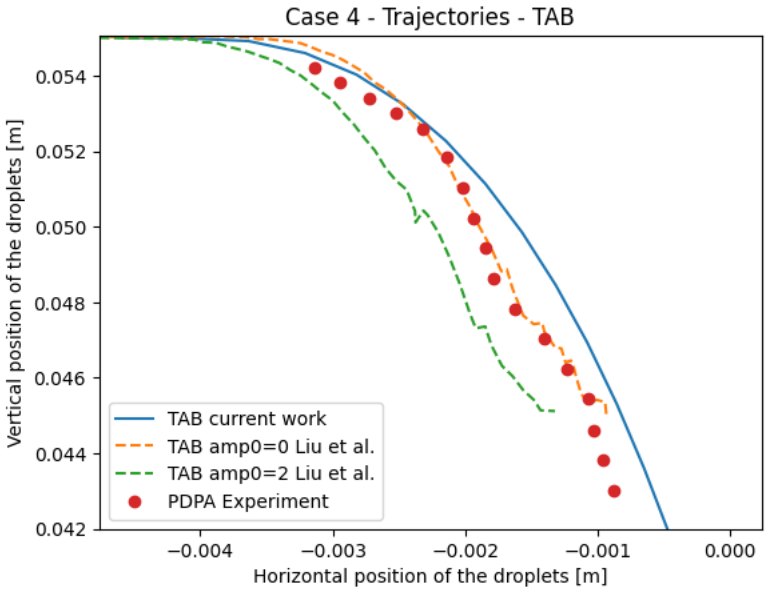

Figure 3.10: Trajectory results from the and TAB-model for the current work and reference data in Case 4.

3.3.4 Conclusion

While some minor misalignment can be observed between our implementation and the extracted from the paper, the simulation of the current work fits quite well in all cases 2, 3, and 4. The key difference among these cases is the air jet velocity, and this leads to several conclusions.

The KH model outperforms the TAB model, particularly in predicting droplet Reynolds fluctuations before the final breakup and the Reynolds number. TAB struggles to accurately capture Reynolds numbers after the breakup.

Regarding trajectory predictions, current work implementation closely matches the trajectories for Case 2, while the KH model shows better results compared to the TAB model. However, as the jet velocity increases, differences between the data and simulations become more apparent, especially in the TAB implementation.

When examining the Sauter mean diameter (SMD) for all three cases, the KH model performs better by predicting the final droplet diameter closer to the actual data. TAB, in general, breaks up faster and to smaller diameters in less steps compared to reality. Additionally, in terms of alignment with the paper's implementation, the KH model is in line with the wave model implementation by Liu et al, specially by using standard drag model.

Chapter 4

Solidification Modelling

4.1 Considerations

As discussed in the section 2.2.4, in the current work, solidification is assumed to happen as a one step phase change. The class sprayCloud was modified to be able to take into account gas, liquid and solid phase in the lagrangian parcels, instead of only liquid. A solidification model was added to this modified sprayCloud class. This function alters the phase of each parcel based on temperature changes and updates parcel properties and dimensions based on that. Liquid and solid iron properties were added to the thermophysical library in order to use the solidification model for iron.

4.1.1 Setup

The setup closely follows that of Liu et al.'s paper. Given that iron is nearly 10 times denser than benz and has different properties, achieving droplet breakup requires setting the initial diameter and jet velocity in a manner such that, around the time of injection, the gas Weber number exceeds the critical value for the KH model. Additionally, it is important to balance the droplet injection velocity to ensure that the droplet remains within the jet domain. Table 4.1 provides a summary of the changes.

By selecting the KH model as the breakup model and employing the Rans-Marshal model for heat exchange, with radiation disabled, the model is now ready. To investigate the influence of solidification, two scenarios is considered: one without solidification and another with the solidification mode activated. The goal is to compare the impact of solidification before the droplet completely breaks up for

Model Specifications		
Air Nozzle	Velocity	450 m/s
Droplet	Diameter	500 µm
Melt	Iron	Fe
	Specifications	
	Density	8711.946 - 0.926 T kg/m^3
	Melting/Solidification point (T_m)	1811 K
Melt Nozzle	Injection Specifications	
	Injection Temperature	1815 K
	Exit Diameter	500 µm
	Injection Velocity	5 m/s

Table 4.1: Solidification model specifications

when $We_g < We_{cr}$ (early solidification[1]) to the case where solidification do not happen. To achieve this, the trajectory and changes in the parent diameter will be examined both before and after activating the solidification function.

4.2 Results

4.2.1 Trajectories

As depicted in Figure 4.1, following the blue line, the trajectory of the Fe parcel deviates noticeably after droplet solidifies. This is attributed to the larger diameter of the solidified parent droplet onward, leading to a higher drag force and weight which then slows down the droplet and curve down trajectory, as anticipated.

4.2.2 SMD vs. Temperature

In Figure 4.2, the red dashed line represents the Iron melting point. On the left y-axis, the blue line illustrates the diameter of the parent droplet when the solidification mode is activated, while the dotted orange line represents the scenario without solidification. On the right y-axis, the green line and purple dotted line

[1]Early solidification, in the context of this thesis, refers to the occurrence of droplet solidification in the atomization process before the breakup process fully reaches the point where breakup no longer occurs.

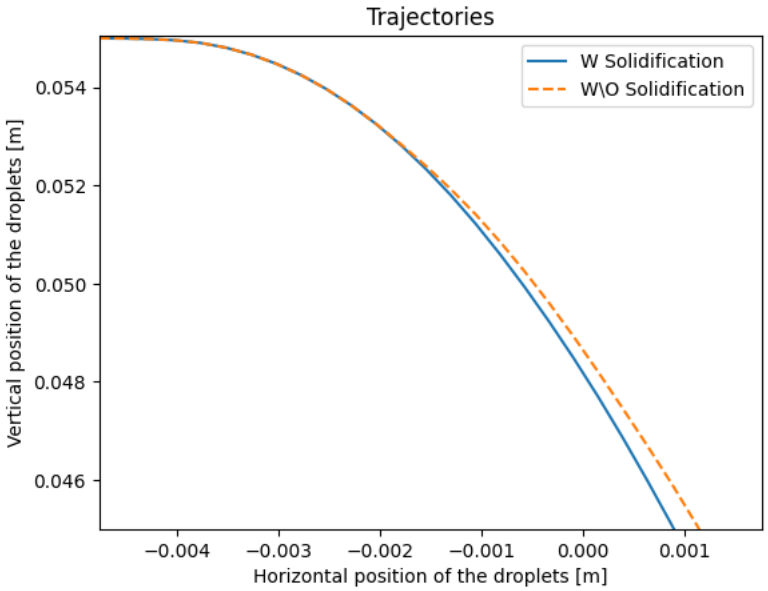

Figure 4.1: Trajectories for Fe droplets with and without solidification.

depict the change in temperature over the horizontal position for the cases with and without solidification, respectively.

Solidification is evident when the decrease in Sauter mean diameter (SMD) of the blue line (with solidification mode on) halts, whereas the orange dotted line, representing the SMD for the case without solidification, continues to decrease, indicating that the droplet still breaks up. This precisely occurs at the point (x = -2.402 mm) where the droplet temperature falls below $T_m = 1811K$. The slight decrease observed after the switch point is attributed to post-processing and SMD calculation and should not be mistaken as a continuation of the breakup process. The temperature rate remains consistent during solidification due to the small size of the droplets and the close proximity of their specific heat capacities, C_p.

4.2.3 Conclusion

Upon looking at Figures 4.1 and 4.2, it can be concluded that the phase change from liquid to solid has occurred successfully. This is evident as the positions at the temperatures corresponding to this transition align with the expected melting temperature.

An important observation, according to Figure 4.2, is the influence of solidification time on the final particle size distribution. Results show that if the droplet solidifies before the gas Weber number reaches its critical value (e.g., when the droplet injection temperature is very close to the melting point), the final diameter

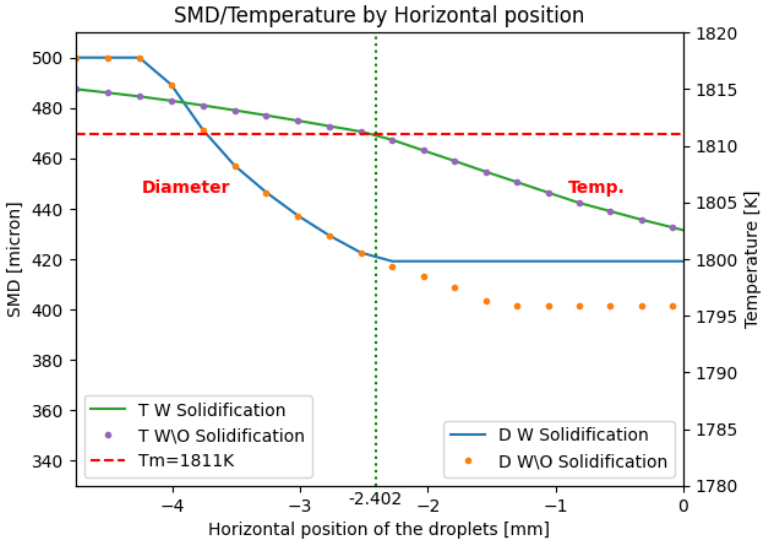

Figure 4.2: SMD and temperature by horizontal position for Fe droplets with and without solidification.

of the droplet remains higher compared to cases where solidification occurs after the droplet breaks up into smaller particles. Therefore, in order to have finer particles at the end, the droplet temperature at the time of injection (gas-melt temperature difference) must provide enough time for most liquid droplets to break up as much as possible.

As discussed in Section 2.2.4, the solidification process occurs earlier and faster in smaller droplets. Allowing the droplet to solidify after more breakup enhances the atomization process, resulting in better distribution and lower costs. Smaller particles experience higher undercooling, leading to larger and sharper recalescence, causing a higher percentage of the liquid droplet to solidify during that phase.

On the other hand, introducing melt with a very high temperature would increase the solidification time, potentially leading to satellite formation due to higher probability of particle collisions. Also, in turn, could result in a higher cost for the atomizer to accommodate more room in the chamber for the solidification process to complete.

Early solidification , as depicted in Figure 4.1, would cause trajectories to deviate from the edges of the spray towards the core. In the presence of a large distribution of parcels, particles would cool more slowly in the core region, as the gas is heated up, compared to the edges where ambient gas is generally colder.

Chapter 5

Epilogue

5.1 Conclusions

In this study, the initial step involves modelling the breakup and trajectory of single drops injected into a high-velocity gas flow, as represented by Liu et al. The implementation is carried out using Lagrangian library of open source CFD sotwate OpenFOAM. The computations for breakup were made using both TAB and KH models for three cases with different gas jet velocities at low Weber numbers. The results are then compared with simulations from the paper using both TAB and Wave models. The accuracy of these models is also assessed by comparison with experimental data in the Lie et al.'s study.

By looking at the results in chapter 3 from the Liu et al.'s paper and the implementation carried out in this thesis, it has been demonstrated that the current work KH and TAB model, built based on class input and adapted for the sprayFoam solver, match well with both KH and TAB models from the paper. Notably, it has been successfully shown that the results obtained using the KH model align well with the PDPA experiments conducted by Liu et al. In fact, the KH model, which computes the breakup of droplets with non-oscillated diameter, aligns well with experimental outcomes.

However, when comparing the results obtained from TAB modeling, it becomes evident that although the the model predicts the trajectories well but it poorly captures the breakup drop sizes compared to the experiment, particularly at higher relative velocities. Therefore, it can be concluded that, for the prediction of breakup phenomena, the KH model provides more accurate results

In the next step, the choice of the KH model for breakup and the selection of iron as the metal droplet were made. Opting for effectively modeling all three phases into sprayCloud class of the Lagrangian library has facilitated working with phase fraction values and maintaining control over parcel properties during solidification

of the droplet. Finally, the solidification function based on temperature change has been implemented. Two cases were considered, one with the effect of solidification and another without. he initial droplet temperature was set to be 4 degrees above the melting point to ensure that the droplet solidifies earlier than all breakups happen for each parcel.

The results obtained from the solidification of droplets have been validated and aligned well with expected outcomes. It has been demonstrated that both the time of solidification and solidification duration are crucial factors for predicting the final size distribution of broken-up droplets. The study found that early solidification can lead to droplets missing the opportunity to break up into finer particles, and it also results in a longer solidification time due to larger droplet dimensions. On the contrary, introducing melt at a high temperature may cause droplets to solidify later than necessary, thereby increasing the energy and cost required to cool down the overheated droplet and melt. Additionally, these factors also provide the temperature at which the melt is introduced, providing an acceptable foundation for progressing toward more refined and accurate models.

5.2 Limits and Recommendations

The Gas Weber number at the time of injection determines whether and how the droplet undergoes the breakup process. Therefore, gas flow conditions, such as the gas velocity profile, are crucial, particularly at the injection position, which, in this case, is at the edge of the gas jet. This is important for accurately predicting the exact behavior of the droplet. As Liu et al.'s paper did not delve into a detailed discussion of the exact gas velocity profile, particularly at the edges, it became crucial to focus on the flow conditions at the injection point.

From the modelling the gas atomization point of view, the assumption of a flat jet profile itself is also a significant factor influencing the accuracy, as it can impact the Weber number of the gas surrounding the droplet, which is directly related to breakup behavior. Another limitation in the model setup stems from the assumption that all child droplets travel within the parcel without the freedom to be extracted from the parcel and move with the jet spray. Hence assigning each droplet to a new and only one parcel would help the accuracy of the model. The injection of uniformly spherical droplets with same velocity further affects the setup and significantly alter the results from real gas atomizer experiments. This assumption not only underestimates complexities such as coupling between primary and secondary breakup but also leads to early solidification of larger drops, resulting in a poor prediction of size distribution. A notable limitation of this implementation arises from the fact that only one droplet in introduced, which simplifies the consideration of its cooling behavior to be similar to the droplets

traveling near the edge of the air jet with certain size distribution. However, in reality, all droplets with different size and shapes are injected into the spray, contributing to the heating of the gas and elongating the solidification rate and time. Additionally, considering the effects like turbulence of gas jet can play a crucial role in modelling cooling, breakup, and other phenomena such as splashing and satellite formation.

The complexity of the Lagrangian library and the highly modular nature of OpenFOAM have constrained the implementation of the dynamics associated with all solidification phases within the scope of this thesis. In general, achieving a finer powder isn't just a desirable end goal from gas atomization viewpoint; it also aids in expediting solidification process, thereby reducing the need for elongating the atomization chamber to accommodate this process. Accordingly, it is essential to model and estimate all stages of solidification.

5.3 Future Research

Due to the complexity of the atomization phenomena, as a further research introducing a non-uniform size distribution of droplets with with different velocities gives a better understanding over the final size distribution.

Another study could focus on the time it takes for droplets with different diameters to break up and reach the same final diameter. This can help estimate the time required for a specific distribution of droplets with various sizes to achieve a desirable final distribution. This time can later be used to calculate the melt temperature, which is related to the initiation of solidification during the atomization process.

Given the dependency of breakup behavior on the gas Weber number, it is valuable to study the effect of different gas jet profiles on the breakup phenomena. This is particularly helpful in understanding whether the gas jet profile contributes to the production of finer droplets. As the droplet breaks up and penetrates into the jet, the expectation is that smaller droplets are produced, and higher jet velocity at further distances is likely to facilitate more breakups.

On the other hand, introducing more droplets, possibly with different sizes, may provide a better understanding of whether turbulence caused by droplets upstream affect the breakup behavior of subsequent droplets.

As discussed in Section 2.2.4, for further research, it is crucial to provide at least an estimate for the different phases of solidification and handle each phase with care. Due to the relatively long process of under-cooling in the liquid droplet (on the order of 10^{-2}s), it is crucial to be incorporated into the simulation. This is particularly significant given that the subsequent stage, recalescence, initiates from the under-cooled nucleation temperature rather than the melting temperature.

Recalescence, a rapid phenomenon responsible for a high percentage of solidification [56], can be approximated through a linear process. In cases where the droplet is sufficiently small, recalescence can occur in a single step, reaching the melting temperature and resembling a switch in the process. Implementing a more complex model might have minimal impact on the final results under these conditions.

It is noteworthy to point out that when the solidification fraction reaches values around 30-40% during recalescence [56], and given that solidification occurs near the droplet's final breakups, the liquid fraction sharply decreases. Consequently, the Weber number for the liquid fraction falls below critical values for sufficiently small droplets, causing the breakup to stop, even though the solidification of the droplet is not yet mature.

The linearization of the segregated solidification after recalescence is possible due to a more stable process. However, it is crucial to note that since collisions may occur between the already solidified smaller child droplets and the liquid phase of the droplet still undergoing segregated solidification, the formation of satellites may need to be considered at this stage.

Bibliography

[1] Alex B. Liu, Daniel Mather, and Rolf D. Reitz. «Modeling the Effects of Drop Drag and Breakup on Fuel Sprays». In: *SAE Transactions* 102 (1993), pp. 83–95. ISSN: 0096736X, 25771531. URL: http://www.jstor.org/stable/44611358 (visited on 09/03/2023) (cit. on pp. i, 29, 32, 33, 40).

[2] Kazybek Kassym and Asma Perveen. «Atomization processes of metal powders for 3D printing». In: *Materials today: proceedings* 26 (2020), pp. 1727–1733 (cit. on pp. 1, 2, 5).

[3] Jun Zhang, Negin Amini, David AV Morton, and Karen P Hapgood. «3D printing with particles as feedstock materials». In: *Advanced Powder Technology* 32.9 (2021), pp. 3324–3345 (cit. on p. 1).

[4] Valmik Bhavar, Prakash Kattire, Vinaykumar Patil, Shreyans Khot, Kiran Gujar, and Rajkumar Singh. «A review on powder bed fusion technology of metal additive manufacturing». In: *Additive manufacturing handbook* (2017), pp. 251–253 (cit. on pp. 1, 2).

[5] Chaolin Tan, Kesong Zhou, Wenyou Ma, Bonnie Attard, Panpan Zhang, and Tongchun Kuang. «Selective laser melting of high-performance pure tungsten: parameter design, densification behavior and mechanical properties». In: *Science and Technology of Advanced Materials* 19.1 (2018). PMID: 29707073, pp. 370–380. DOI: 10.1080/14686996.2018.1455154 (cit. on pp. 1, 2).

[6] HP Tang, Ma Qian, N Liu, XZ Zhang, GY Yang, and J Wang. «Effect of powder reuse times on additive manufacturing of Ti-6Al-4V by selective electron beam melting». In: *Jom* 67.3 (2015), pp. 555–563 (cit. on p. 2).

[7] Thomas Duda and L Venkat Raghavan. «3D metal printing technology». In: *IFAC-PapersOnLine* 49.29 (2016), pp. 103–110 (cit. on p. 2).

[8] GSE Antipas. «Review of gas atomisation and spray forming phenomenology». In: *Powder Metallurgy* 56.4 (2013), pp. 317–330 (cit. on pp. 2, 3, 5).

[9] Stanislav Lagutkin, Lydia Achelis, Sheikhali Sheikhaliev, Volker Uhlenwinkel, and Vikas Srivastava. «Atomization process for metal powder». In: *Materials Science and Engineering: A* 383.1 (2004). 2nd International Conference on Spray Deposition and Melt Atomization and the 5th International Conference on Spray Forming, pp. 1–6. ISSN: 0921-5093. DOI: https://doi.org/10.1016/j.msea.2004.02.059 (cit. on pp. 3, 5).

[10] Chang LIU, Xin LI, Shi SHU, Yu-he HUANG, Xing-gang LI, and Qiang ZHU. «Numerical investigation on flow process of liquid metals in melt delivery nozzle during gas atomization process for fine metal powder production». In: *Transactions of Nonferrous Metals Society of China* 31.10 (2021), pp. 3192–3204. ISSN: 1003-6326. DOI: https://doi.org/10.1016/S1003-6326(21)65725-4 (cit. on pp. 3, 5).

[11] Leo V. M. Antony and Ramana G. Reddy. «Processes for the Production of High-Purity Metal Powders». In: *Journal of Materials (JOM)* 55.3 (2003), pp. 14–18. ISSN: 1543-1851. DOI: 10.1007/s11837-003-0153-4. URL: https://doi.org/10.1007/s11837-003-0153-4 (cit. on pp. 3, 5).

[12] J.J. Dunkley. «1 - Advances in atomisation techniques for the formation of metal powders». In: *Advances in Powder Metallurgy*. Ed. by Isaac Chang and Yuyuan Zhao. Woodhead Publishing Series in Metals and Surface Engineering. Woodhead Publishing, 2013, pp. 3–18. ISBN: 978-0-85709-420-9. DOI: https://doi.org/10.1533/9780857098900.1.3. URL: https://www.sciencedirect.com/science/article/pii/B9780857094209500015 (cit. on pp. 3, 5).

[13] R.M. German. *Powder Metallurgy Science*. Metal Powder Industries Federation, 1984. ISBN: 9780918404602. URL: https://books.google.nl/books?id=UYd9QgAACAAJ (cit. on p. 4).

[14] Inc Graco. «Atomization concept and theory». In: *Available from: . Access in:* (2014). URL: http://wwwd.graco.com/training/concept_and_theory/Atomization%20v2.pdf (cit. on p. 4).

[15] S Grenier and F Allaire. «Plasma atomization gives unique spherical powders». In: *Metal Powder Report* 52.11 (1997), pp. 34–37 (cit. on p. 4).

[16] S Özbilen. «Satellite formation mechanism in gas atomised powders». In: *Powder metallurgy* 42.1 (1999), pp. 70–78 (cit. on p. 3).

[17] Zackary Snow, Richard Martukanitz, and Sanjay Joshi. «On the development of powder spreadability metrics and feedstock requirements for powder bed fusion additive manufacturing». In: *Additive Manufacturing* 28 (2019), pp. 78–86 (cit. on p. 4).

[18] Stefan Wallner. «Production methods for producing metal powders». In: *BHM Berg-und Hüttenmännische Monathefte* 164 (2019), pp. 108–111 (cit. on p. 5).

[19] Jason Ting, Michael W Peretti, and William B Eisen. «The effect of wake-closure phenomenon on gas atomization performance». In: *Materials Science and Engineering: A* 326.1 (2002), pp. 110–121 (cit. on p. 6).

[20] N Zeoli and S Gu. «Computational simulation of metal droplet break-up, cooling and solidification during gas atomisation». In: *Computational materials science* 43.2 (2008), pp. 268–278 (cit. on pp. 6, 15).

[21] Xing-gang Li and Udo Fritsching. «Process modeling pressure-swirl-gas-atomization for metal powder production». In: *Journal of Materials Processing Technology* 239 (2017), pp. 1–17 (cit. on pp. 6, 7).

[22] Martin Heinrich and Rüdiger Schwarze. «3D-coupling of Volume-of-Fluid and Lagrangian particle tracking for spray atomization simulation in OpenFOAM». In: *SoftwareX* 11 (2020), p. 100483 (cit. on pp. 6, 14).

[23] Mingming Tong and David J Browne. «Direct numerical simulation of melt–gas hydrodynamic interactions during the early stage of atomisation of liquid intermetallic». In: *Journal of Materials Processing Technology* 202.1-3 (2008), pp. 419–427 (cit. on p. 6).

[24] Rasmus Gjesing, Jesper Hattel, and Udo Fritsching. «Coupled atomization and spray modelling in the spray forming process using open foam». In: *Engineering Applications of Computational Fluid Mechanics* 3.4 (2009), pp. 471–486 (cit. on p. 6).

[25] N Zeoli, H Tabbara, and S Gu. «CFD modeling of primary breakup during metal powder atomization». In: *Chemical engineering science* 66.24 (2011), pp. 6498–6504 (cit. on pp. 7, 8).

[26] Dudi Adi Firmansyah, Rashed Kaiser, Riyan Zahaf, Zach Coker, Tae-Youl Choi, and Donggeun Lee. «Numerical simulations of supersonic gas atomization of liquid metal droplets». In: *Japanese Journal of Applied Physics* 53.5S3 (2014), 05HA09 (cit. on pp. 7, 8, 12).

[27] J S Thompson, Oubay Hassan, SA Rolland, and Johann Sienz. «The identification of an accurate simulation approach to predict the effect of operational parameters on the particle size distribution (PSD) of powders produced by an industrial close-coupled gas atomiser». In: *Powder Technology* 291 (2016), pp. 75–85 (cit. on pp. 7, 9, 12).

[28] Maria Rita Ridolfi and Paolo Folgarait. «Numerical modeling of secondary breakup in molten metals gas-atomization using dimensionless analysis». In: *International Journal of Multiphase Flow* 132 (2020), p. 103431 (cit. on p. 7).

[29] Rashed Kaiser, Chengguo Li, Sangsun Yang, and Donggeun Lee. «A numerical simulation study of the path-resolved breakup behaviors of molten metal in high-pressure gas atomization: With emphasis on the role of shock waves in the gas/molten metal interaction». In: *Advanced Powder Technology* 29.3 (2018), pp. 623–630 (cit. on p. 8).

[30] N Zeoli, H Tabbara, and S Gu. «Three-dimensional simulation of primary break-up in a close-coupled atomizer». In: *Applied Physics A* 108 (2012), pp. 783–792 (cit. on p. 9).

[31] SV Apte, Mikhael Gorokhovski, and Parviz Moin. «LES of atomizing spray with stochastic modeling of secondary breakup». In: *International Journal of Multiphase Flow* 29.9 (2003), pp. 1503–1522 (cit. on p. 8).

[32] J Shinjo and A Umemura. «Simulation of liquid jet primary breakup: Dynamics of ligament and droplet formation». In: *International journal of multiphase Flow* 36.7 (2010), pp. 513–532 (cit. on p. 8).

[33] Wenjun Zhao, Fuyang Cao, Zhiliang Ning, Guoqing Zhang, Zhou Li, and Jianfei Sun. «A computational fluid dynamics (CFD) investigation of the flow field and the primary atomization of the close coupled atomizer». In: *Computers & chemical engineering* 40 (2012), pp. 58–66 (cit. on pp. 8, 9).

[34] Stefan Markus, Udo Fritsching, and Klaus Bauckhage. «Jet break up of liquid metal in twin fluid atomisation». In: *Materials Science and Engineering: A* 326.1 (2002), pp. 122–133 (cit. on p. 10).

[35] Jeremiah U Brackbill, Douglas B Kothe, and Charles Zemach. «A continuum method for modeling surface tension». In: *Journal of computational physics* 100.2 (1992), pp. 335–354 (cit. on p. 10).

[36] M van Sint Annaland, NG Deen, and JAM Kuipers. «Numerical simulation of gas bubbles behaviour using a three-dimensional volume of fluid method». In: *Chemical engineering science* 60.11 (2005), pp. 2999–3011 (cit. on p. 11).

[37] DR Guildenbecher, C López-Rivera, and PE Sojka. «Secondary atomization». In: *Experiments in Fluids* 46.3 (2009), pp. 371–402 (cit. on pp. 11, 12).

[38] T Hopfes, J Petersen, Z Wang, M Giglmaier, and NA Adams. «Secondary atomization of liquid metal droplets at moderate Weber numbers». In: *International Journal of Multiphase Flow* 143 (2021), p. 103723 (cit. on p. 11).

[39] Peter J O'Rourke and Anthony A Amsden. *The TAB method for numerical calculation of spray droplet breakup*. Tech. rep. SAE technical paper, 1987 (cit. on pp. 12, 18, 19, 31).

[40] Kalpana Hanthanan Arachchilage, Majid Haghshenas, Sharon Park, Le Zhou, Yongho Sohn, Brandon McWilliams, Kyu Cho, and Ranganathan Kumar. «Numerical simulation of high-pressure gas atomization of two-phase flow: Effect of gas pressure on droplet size distribution». In: *Advanced Powder Technology* 30.11 (2019), pp. 2726–2732 (cit. on p. 12).

[41] Holger Grosshans, R-Z Szász, and Laszlo Fuchs. «Development of an efficient statistical volumes of fluid–Lagrangian particle tracking coupling method». In: *International Journal for Numerical Methods in Fluids* 74.12 (2014), pp. 898–918 (cit. on pp. 13, 14).

[42] Marcus Herrmann. «A parallel Eulerian interface tracking/Lagrangian point particle multi-scale coupling procedure». In: *Journal of computational physics* 229.3 (2010), pp. 745–759 (cit. on pp. 13, 14).

[43] N Ciftci, N Ellendt, G Coulthard, E Soares Barreto, L Mädler, and V Uhlenwinkel. «Novel cooling rate correlations in molten metal gas atomization». In: *Metallurgical and Materials Transactions B* 50 (2019), pp. 666–677 (cit. on p. 15).

[44] Jesper Henri Hattel, Nini H Pryds, Jesper Thorborg, and Preben Ottosen. «A quasi-stationary numerical model of atomized metal droplets. I: Model formulation». In: *Modelling and Simulation in Materials Science and Engineering* 7.3 (1999), p. 413 (cit. on p. 15).

[45] Douglas Hector Fontes, Vitor Vilela, Lucas de Souza Meira, and Francisco Jose de Souza. «Improved hybrid model applied to liquid jet in crossflow». In: *International Journal of Multiphase Flow* 114 (2019), pp. 98–114 (cit. on p. 19).

[46] Ming-Chia Lai, Fu-Quan Zhao, Amer Ahmad Amer, and Tsan-Hai Chue. «An experimental and analytical investigation of the spray structure from automotive port injectors». In: *SAE transactions* (1994), pp. 833–852 (cit. on p. 20).

[47] Min Xu and Lee E Markle. «CFD-aided development of spray for an outwardly opening direct injection gasoline injector». In: *SAE transactions* (1998), pp. 486–497 (cit. on p. 20).

[48] Jian-Rong Qin, Tomohisa Dan, Ming-Chia Lai, Craig Savonen, Ernest Schwartz, and Walter Brkyzik. «Correlating the diesel spray behavior to nozzle design». In: *SAE transactions* (1999), pp. 1726–1738 (cit. on p. 20).

[49] RD Reitz. «Encyclopedia of fluid mechanics». In: *Gulf Pub* 3 (1986), pp. 233–249 (cit. on p. 21).

[50] Rolf D Reitz. «Mechanism of breakup of round liquid jets». In: *Encyclopedia of fluid mechanics* 10 (1986) (cit. on p. 21).

[51] Rolfd Reitz et al. «Modeling atomization processes in high-pressure vaporizing sprays». In: *Atomisation and Spray technology* 3.4 (1987), pp. 309–337 (cit. on pp. 22, 24, 25, 31).

[52] Russell James Donnelly and W Glaberson. «Experiments on the capillary instability of a liquid jet». In: *Proceedings of the Royal Society of London. Series A. Mathematical and Physical Sciences* 290.1423 (1966), pp. 547–556 (cit. on p. 24).

[53] Anthony A Amsden, Peter J O'Rourke, and T Daniel Butler. *KIVA-II: A computer program for chemically reactive flows with sprays*. Tech. rep. Los Alamos National Lab.(LANL), Los Alamos, NM (United States), 1989 (cit. on p. 26).

[54] Geoffrey Ingram Taylor. «The shape and acceleration of a drop in a high speed air stream». In: *The Scientific Papers of G.. I. Taylor* (1963) (cit. on p. 26).

[55] Yunfei Hu, Xiang-lin Zhou, Liang-hui Xu, Jing-hao Li, Hang Qi, Kai-ping Du, Yao Ma, and Yue-guang Yu. «Motion and solidification behavior analysis of Fe-based alloy droplets during gas atomization». In: *Metallurgical and Materials Transactions B* 51 (2020), pp. 2935–2945 (cit. on p. 27).

[56] Dirk Bergmann, Udo Fritsching, and Klaus Bauckhage. «A mathematical model for cooling and rapid solidification of molten metal droplets». In: *International journal of thermal sciences* 39.1 (2000), pp. 53–62 (cit. on pp. 27–29, 51).

[57] James Arthur Nicholls and AA Ranger. «Aerodynamic shattering of liquid drops.» In: *Aiaa Journal* 7.2 (1969), pp. 285–290 (cit. on p. 31).

[58] Manuel A Gonzalez D, Zhi W Lian, and Rolf D Reitz. «Modeling diesel engine spray vaporization and combustion». In: *SAE transactions* (1992), pp. 1064–1076 (cit. on p. 31).

[59] Ewe Wei Saw. «Studies of spatial clustering of inertial particles in turbulence». In: (Jan. 2008) (cit. on p. 33).